CsCl Seed Layer Strategy for Enhanced Fabrication Yield and Device Performance of Solution-Based Two-Step Processed Perovskite Solar Cells

Ronja Pappenberger[1,2], Alexander Diercks[2], Roja Singh[1,2], Alexander Welle[3,4], Tonghan Zhao[1], Julian Petry[1,2], and Ulrich W. Paetzold[1,2]

[1]Institute of Microstructure Technology (IMT), Karlsruhe Institute of Technology (KIT), Hermann-von-Helmholtz-Platz 1, 76344 Eggenstein-Leopoldshafen, Germany
[2]Light Technology Institute (LTI), Karlsruhe Institute of Technology (KIT), Engesserstrasse 13, 76131 Karlsruhe, Germany
[3]Institute of Functional Interfaces (IFG), Karlsruhe Institute of Technology (KIT), Hermann-von-Helmholtz-Platz 1, 76344 Eggenstein-Leopoldshafen, Germany
[4]Karlsruhe Nano Micro Facility (KNMFi), Karlsruhe Institute of Technology (KIT), Hermann-von-Helmholtz-Platz 1, 76344 Eggenstein-Leopoldshafen, Germany

E-Mail:
ronja.pappenberger@kit.edu; ulrich.paetzold@kit.edu

Keywords: perovskite solar cell, sequential deposition, seed layer, 2T tandem solar cell

Abstract

Inverted perovskite solar cells (PSCs) are promising top-cell candidates for 2T perovskite/silicon tandem devices; however, achieving uniform and defect-free perovskite coverage on industrially relevant textured silicon bottom cells remains a major challenge for conventional solution-based perovskite deposition. Here, we introduce a vapor-deposited CsCl seed layer at the hole transport layer/perovskite interface in a solution-based two-step deposition method. This strategy promotes nucleation and improves perovskite film formation, particularly in regions where solution processing alone is insufficient. When implemented in wide-bandgap (E_g = 1.67 eV) *p-i-n* PSCs, the approach significantly enhances device performance and long-term operational stability, achieving power conversion efficiencies of 19% and retaining 83% of initial device performance after 1000 h of continuous illumination at 25 °C in a nitrogen atmosphere. In 2T perovskite/silicon tandem architectures, the CsCl seed layer strategy markedly enhances process repeatability and fabrication yield – particularly on textured silicon bottom cells – achieving yields exceeding 70% across different silicon bottom cell surface structures. These findings demonstrate a simple and scalable strategy to improve the reliability of perovskite film formation, supporting the industrial implementation of 2T perovskite/silicon tandem solar cells.

1 Introduction

Organic-inorganic hybrid perovskite solar cells (PSCs) have emerged as promising candidates for next-generation photovoltaics (PV), with power conversion efficiencies (PCEs) increasing from 3.8% in 2009 to 27.3% today, approaching those of state-of-the-art silicon (Si) solar cells.[1,2] In particular, inverted PSCs (*p-i-n* architecture) are highly attractive for 2T perovskite/Si tandem solar cells (TSCs), enabling efficiencies beyond the practical crystalline single-junction Si limit of 29%[3] and reaching record values of up to 35%.[2] Commercial Si bottom cells typically feature micrometer-scale random pyramidal textures ($\approx$ 2 to 5 µm in height), which enhance light incoupling and reduce reflection losses compared to planar surfaces.[4–9] However, achieving uniform and defect-free perovskite coverage on such pronounced textures remains a major challenge for conventional solution-based deposition methods. Incomplete film coverage can lead to thickness inhomogeneities and shunting pathways, severely degrading device performance and fabrication yield.[10,11] Vapor-phase deposition methods offer conformal coverage, but often suffer from limited device performance and poor process repeatability due to the complexity of multi-source deposition and the volatile nature of organic components.[12–17]

Among various deposition techniques, the solution-based two-step deposition method – comprising the subsequent deposition of the Pb-containing precursor materials and the organic cations – has emerged as a promising route to process uniform and high-quality perovskite thin films.[18–21] This method is compatible with large-area deposition techniques such as vapor-phase deposition,[22] slot-die coating[23] and ink-jet printing[24,25], as well as hybrid deposition routes that combine vapor- and solution-based deposition.[10,26–31]

In a previous work, we demonstrated the general compatibility of the solution-based two-step method with different textured Si bottom cells.[21] Nevertheless, incomplete coverage and limited process repeatability persist, highlighting the need for additional strategies to control nucleation and perovskite film formation on complex surface topographies.

One promising strategy to improve perovskite film formation is the incorporation of alkali halides such as CsCl into the inorganic scaffold, which can promote crystallization and enhance perovskite film quality.[32] However, the poor solubility of CsCl in commonly used solvents (DMF/DMSO) hinders its direct incorporation into solution-based precursors. As an alternative, CsCl can be introduced *via* vapor-phase deposition as a seed layer at the hole transport layer (HTL)/perovskite interface. Previous studies have demonstrated that CsBr seed layers can improve perovskite film formation and reduce residual PbI_2 in hybrid-deposited perovskite films for textured 2T perovskite/Si TSCs,[27] while CsCl seed layers in co-sublimated perovskite films have shown beneficial effects on crystallization and bandgap control for single-junction and tandem devices.[33,34] However, the role of a CsCl seed layer in solution-processed wide-bandgap PSCs – particularly regarding fabrication yield on textured Si bottom cells – remains unexplored.

In this study, a solution-based two-step method is used to fabricate wide-bandgap (E_g = 1.67 eV) single-junction PSCs in the *p-i-n* architecture. A 5 nm CsCl seed layer is introduced at the HTL/perovskite interface and subtly modifies perovskite film morphology and crystallization, resulting in a champion power conversion efficiency (PCE) of 19% with significantly improved fill factor (FF) and enhanced operational long-term stability. After 1000 h of continuous light exposure at 25 °C in a nitrogen atmosphere the devices retain 84% of their initial device performance. Importantly, the CsCl seed layer significantly improves process repeatability and fabrication yield on textured Si bottom cells, underscoring its potential for scalable and industrially relevant fabrication of PSCs and 2T perovskite/Si TSCs.

2 Results and Discussion

The solution-based two-step deposition method used to fabricate the perovskite thin films in this study is schematically illustrated in Figure 1. The sequential deposition of the inorganic precursors and the organic precursors as well as the double-cation (DC) perovskite composition, $Cs_{0.16}FA_{0.84}Pb(I_{0.79}Br_{0.21})_3$, with a bandgap of 1.67 eV are adopted from a previous study [21] and the corresponding devices are labeled as reference (Ref, blue frame in Figure 1). Introducing a vapor-deposited CsCl seed layer before the inorganic scaffold deposition leads to the devices labeled as CsCl (orange frame in Figure 1). Both – Ref and CsCl PSCs – use a combination of propane-1,3-diammonium iodide ($PDAI_2$) and n-butylammonium iodide (BAI) as bulk and surface passivation. The device architecture (*p-i-n*) of the PSCs consists of the layer stack ITO/NiO_x/2PACz/(CsCl)/perovskite/$PDAI_2$+BAI/C_{60}/SnO_2/Ag and is presented in Figure 2a. The NiO_x/2PACz bilayer serves as the *p*-selective contact, which has been shown to improve both hole extraction and perovskite film quality compared to devices using 2PACz alone. [35] Further details on the fabrication method of the PSCs are described in the Experimental Section.

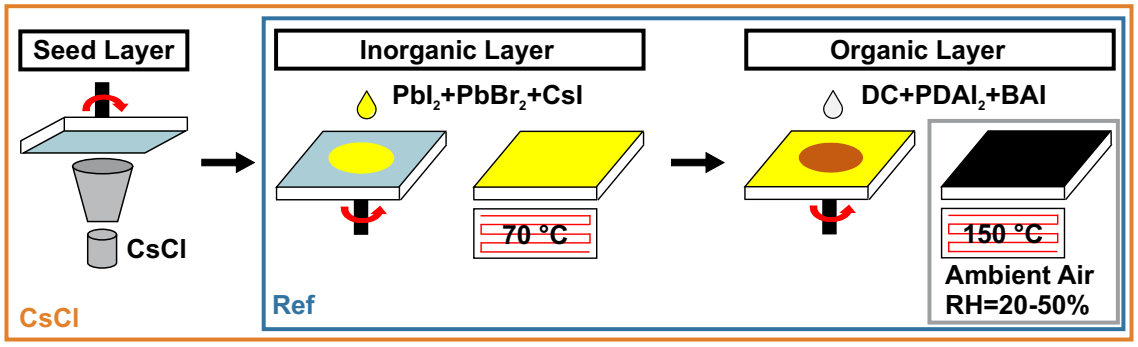

Figure 1: Schematic illustration of the solution-based two-step deposition method used in this study to fabricate perovskite films. Reference (Ref) devices follow an established route adapted from a previous work, [21] while CsCl devices include a 5 nm thin CsCl seed layer (introduced *via* vapor deposition) at the hole transport layer/perovskite interface. The organic cation solution is based on a previously established double-cation (DC) recipe [21] with FAI, FABr and MACl. Propane-1,3-diammonium iodide ($PDAI_2$) and n-butylammonium iodide (BAI) are used as bulk and surface passivation.

2.1 Photovoltaic Performance of Perovskite Solar Cells

Introducing a 5 nm CsCl seed layer at the HTL/perovskite interface proves to be an effective strategy for high-performance *p-i-n* type PSCs.

A pronounced increase in FF and a reduced hysteresis are observed for CsCl devices in the current density-voltage (J–V) characteristics and PV parameters of the best-performing cells (Figure 2b, Table S1, and Figure S1b). The improvement in FF is primarily attributed to an increase in shunt resistance, likely resulting from the insulating nature of the thin CsCl interlayer, which suppresses shunt pathways. A similar FF enhancement was previously reported by Li *et al.* [27] using a CsBr seed layer in a hybrid two-step deposition method. As a result, CsCl devices achieve a champion performance of 19.0% in the backward scan (18.0% in the forward scan) with an open-circuit voltage (V_{OC}) of 1.20 (1.20) V, a short-current density (J_{SC}) of 19.7 (19.7) mA/cm^2, and a FF of 80.4% (76.4%). Statistical analysis based on *Welch's t-test* [36] confirms that the FF improvement, and thus the PCE improvement, is statistically significant (Table S2).

The statistical PV performance in the backward scan (Figure 2c) indicates a slight increase in J_{SC} for CsCl devices, although this trend is not reflected in the external quantum efficiency (EQE) spectra (Figure S1c). The small amount of Cl introduced by the CsCl seed layer does not lead to measurable bandgap changes (Figure S1d), and the absorption spec-

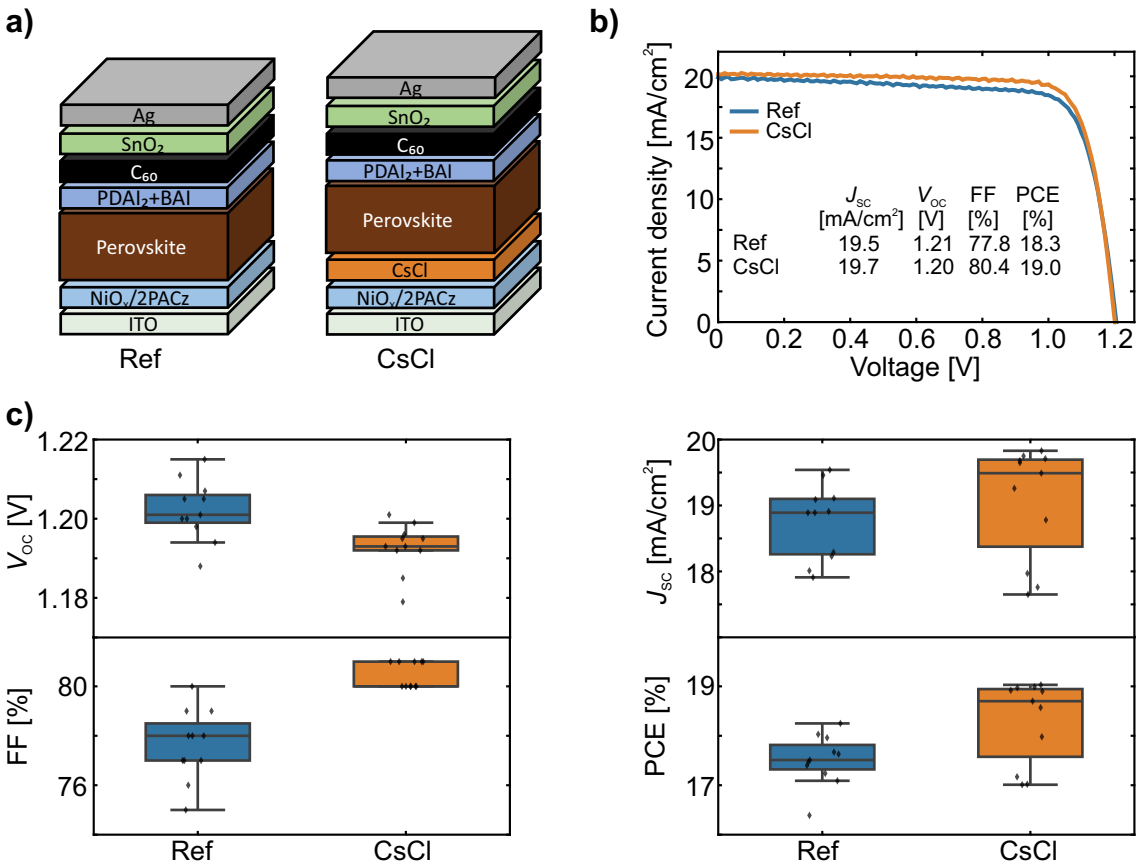

Figure 2: a) Schematic of the perovskite solar cell (PSC) architecture (*p-i-n* architecture). b) Current density *versus* voltage (J–V) characteristics and c) statistical distribution (in total 22 devices) of the open-circuit voltage (V_{OC}), fill factor (FF), short-circuit current density (J_{SC}) and power conversion efficiency (PCE) of opaque PSCs without any further modification (Ref) and with 5 nm CsCl seed layer (CsCl).

tra remain comparable for both devices (Figure S1e). These observations suggest small improvements in charge-carrier extraction rather than changes in optical properties.
Despite the improved charge-carrier extraction and enhanced FF, the V_{OC} decreases by $\approx$ 9 mV compared to Ref PSCs. Possible reasons for this reduction are discussed in the following section.

2.2 Material Characteristics

The morphology and microstructure of both the inorganic scaffold and the final perovskite film are largely unaffected by the introduction of a CsCl seed layer, showing only minor, but beneficial, differences.
The surface morphology of the inorganic scaffolds and perovskite films is characterized by scanning electron microscopy (SEM) and atomic force microscopy (AFM) (Figure 3a-d, Figure S2, Figure S3 and Figure S4). SEM images show that both inorganic scaffolds exhibit a porous structure with visible pinholes. However, the introduction of a CsCl seed layer markedly reduces the pinhole density by approximately a factor of two, accompanied by a shift from large, interconnected voids to smaller and more isolated pinholes. This observation is in agreement with the slightly reduced root-mean-square (RMS) surface roughness measured by AFM compared to the Ref inorganic scaffold (Figure S4). A porous inorganic scaffold can be beneficial as it facilitates infiltration of the organic precursor solution and promotes complete conversion to the perovskite phase.[24] However, a lower pinhole density reduces the number of possible defect sites in the final perovskite film. The resulting perovskite films retain a similar surface morphology, but show a modest

grain size increase – from 364 nm for Ref to 396 nm for CsCl perovskite films (Figure S3). This is consistent with a small reduction in the full width at half maximum (FWHM) of the (100) perovskite diffraction peak (Figure S5b), suggesting improved crystallinity of the CsCl perovskite film.

X-ray diffraction (XRD) measurements (Figure 3e/f and Figure S5a) confirm that Ref and CsCl inorganic scaffolds and perovskite films exhibit the same diffraction peaks and comparable residual PbI_2 content in the final perovskite film, though CsCl perovskite films display a slightly more pronounced (111) crystal orientation. A dominant (111) crystal orientation has been previously linked to enhanced long-term stability,[37] which will be elaborated in more detail in the subsequent discussion. For the CsCl inorganic scaffold, no diffraction peak associated with CsCl is detected, indicating that the CsCl seed layer does not form a separate crystalline phase within the inorganic scaffold or is likely too thin to be detected by XRD. This suggests that CsCl acts primarily as an interfacial modifier rather than contributing to the crystalline structure of the inorganic scaffold.

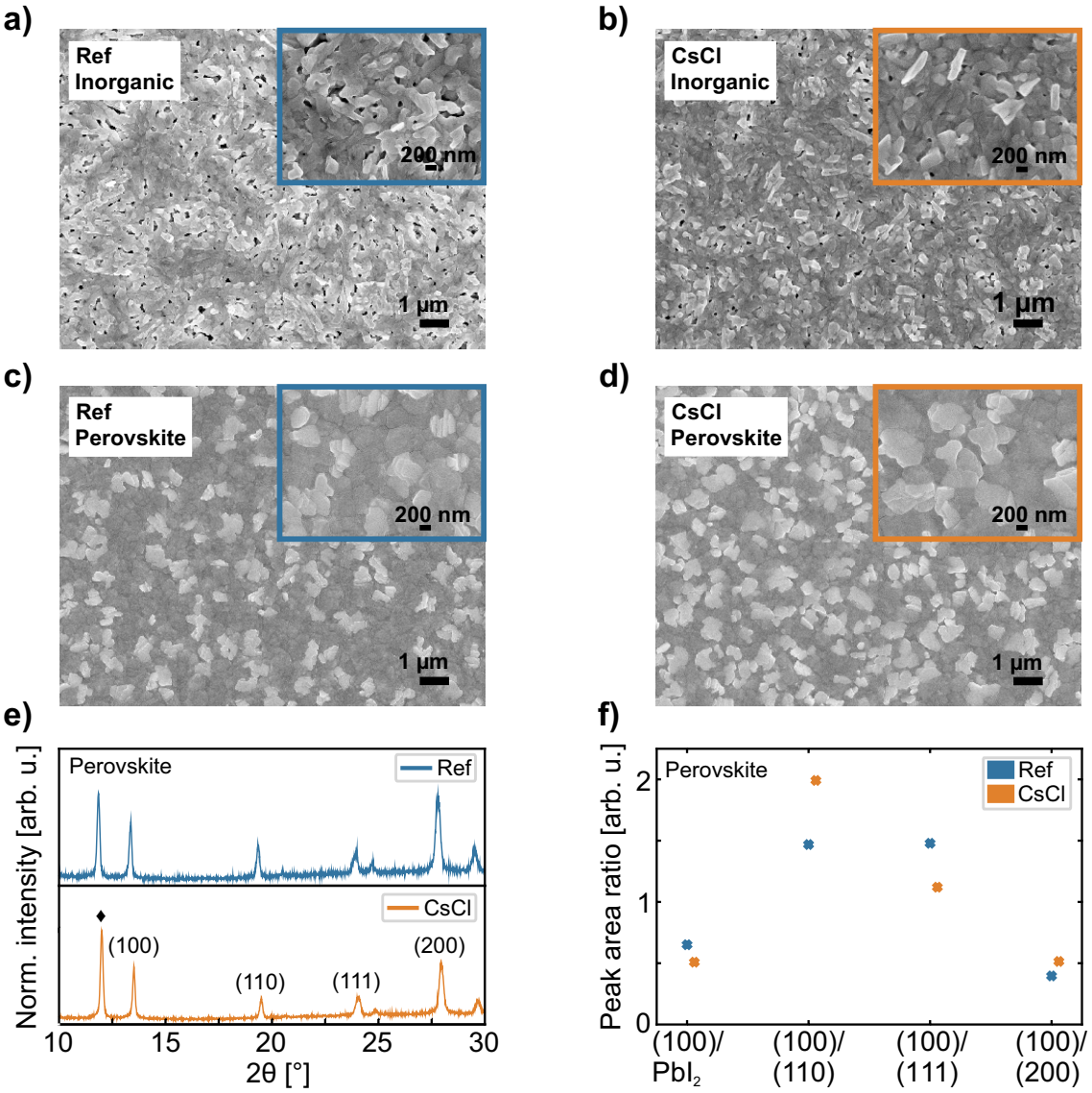

Figure 3: Representative top-view scanning electron microscopy (SEM) images of a/b) inorganic scaffolds and c/d) perovskite films without any further modification (Ref) and with 5 nm CsCl seed layer (CsCl). c) X-ray diffraction (XRD) pattern (♦ denotes the (001) PbI_2 phase) and d) peak area ratios of the XRD patterns for Ref and CsCl perovskite films. The inorganic scaffolds and perovskite films are prepared on ITO/NiO_x/2PACz substrates. The perovskite films are without surface passivation.

Grazing-incidence wide-angle X-ray scattering (GIWAXS) measurements of the inorganic scaffolds and perovskite films corroborate the XRD results and support the assumption of a comparable crystal orientation for both Ref and CsCl configurations (Figure S6). The (001) PbI_2 crystal plane in the inorganic scaffold is unaffected by the CsCl seed layer (Figure S7a). Both Ref and CsCl inorganic scaffolds exhibit a selective out-of-plane orientation, corresponding to a horizontal layer growth of PbI_2 platelets. This growth mode represents the intrinsic growth mode of pure PbI_2 deposited *via* spin coating.[38] The (100) perovskite peak in CsCl perovskite films exhibits a narrower scattering distribution at 60° compared to Ref perovskite films (Figure S7b), indicating a more uniform crystal orientation. This suggests that the CsCl seed layer promotes controlled nucleation and reduces orientation disorder within the perovskite film.

To probe the qualitative elemental distribution as a function of depth, a series of time-of-flight secondary ion mass spectrometry (ToF-SIMS) depth profiles are conducted. Characteristic negatively charged secondary ions of the relevant species for the final PSCs are displayed in Figure S8. Both PSCs – Ref and CsCl – show a nearly identical elemental distribution throughout the whole layer stack. Interestingly, Cl is present in both perovskite films, highlighting that Cl introduced *via* MACl not only acts as an additive during perovskite film formation, but incorporates into the perovskite bulk. The ToF-SIMS measurements do not clearly indicate whether MA is present in the final perovskite film, as CN is a fragment of both FA and MA.

Photoluminescence quantum yield (PLQY) measurements (Figure S9) provide insights into the V_{OC} loss of CsCl devices observed in the PV parameters (Figure 2c). CsCl perovskite films without a C_{60} electron transport layer (ETL) exhibit a reduced PLQY and implied V_{OC} (V_{OC-imp}), accompanied by an increased ideality factor (n_{id}, 1.29 for CsCl *vs.* 1.20 for Ref), indicating less favorable bulk properties. Upon introducing the C_{60} ETL, both PLQY and V_{OC-imp} values exceed those of Ref perovskite films, suggesting improved interfacial quality at the perovskite/C_{60} interface. Together with the reduced hysteresis, this indicates that CsCl primarily enhances interfacial properties. However, the further increase in n_{id} (1.35 for CsCl *vs.* 1.20 for Ref) points to persistent bulk non-radiative recombination losses.

Altogether, materials characterization demonstrates that the CsCl seed layer preserves perovskite film quality while subtly influencing microstructural features in a beneficial manner.

2.3 Long-Term Operational Stability

In order to understand the degradation mechanisms triggered by different stress factors, three standardized tests are chosen for understanding the role of light (ISOS-L1: 100 mW/cm^2, 25 °C, MPP tracking), dark storage (ISOS-D1: dark, 25 °C, intermittent *J*-*V*) and elevated temperatures (ISOS-D2: dark, 85 °C, intermittent *J*-*V*) on PSCs.[39] Semitransparent devices with the layer stack glass/ITO/NiO_x/2PACz/(CsCl)/perovskite/$PDAI_2$+BAI/C_{60}/SnO_x/IZO/Au are exposed to the test conditions.

To examine the effect of dark storage on stability, semitransparent devices are stored under ISOS-D1 test conditions for 1000 h. The normalized PCE from intermittent *J*–*V* measurements for Ref and CsCl PSCs is shown in Figure 4a and the PV parameters before and after the measurement are listed in Table S3. Both – Ref and CsCl – show stable performance over 1000 h. Ref devices retain 94.1% of their initial efficiency, while CsCl devices maintain 99.8%. As shown in Figure S10 the small efficiency loss in Ref devices is mainly due to a decrease in FF and J_{SC}, with V_{OC} remaining stable in both cases.

Accelerated aging under ISOS-D2 test conditions for 1000 h reveals a strong thermal degradation effect (Figure 4b, Table S4), with both device configurations reaching T_{80} within the first 100 h. After 1000 h, Ref devices retain only 14.4% of their initial efficiency, and CsCl devices 15.6%. Considering the remaining device parameters, Figure S11 reveals that the decrease in FF and J_{SC} is the primary cause of PCE loss, while the V_{OC}

declines by less than 10%. Literature reports link prolonged high-temperature exposure (> 500 h) to increased non-radiative recombination within the perovskite layer or at the charge transport layer interfaces, ultimately lowering FF and V_{OC}.[40–42]
To evaluate the operational stability of the PSCs not only under dark storage conditions but also under light exposure, the semitransparent PSCs are subjected to ISOS-L1 test conditions for 1000 h (Figure 4c, Table S5). CsCl devices display the most stable performance, retaining 83% of their initial device performance after 1000 h, outperforming Ref devices. The Ref devices reach T_{80} after 670 h before stabilizing near this value and retain 78% of their initial device performance after 1000 h. Both device configurations show a light-soaking effect during the first 2 h. Analyzing the remaining device parameters (Figure S12) indicates that efficiency loss is primarily driven by reduced J_{SC}, with V_{OC} remaining largely unaffected.

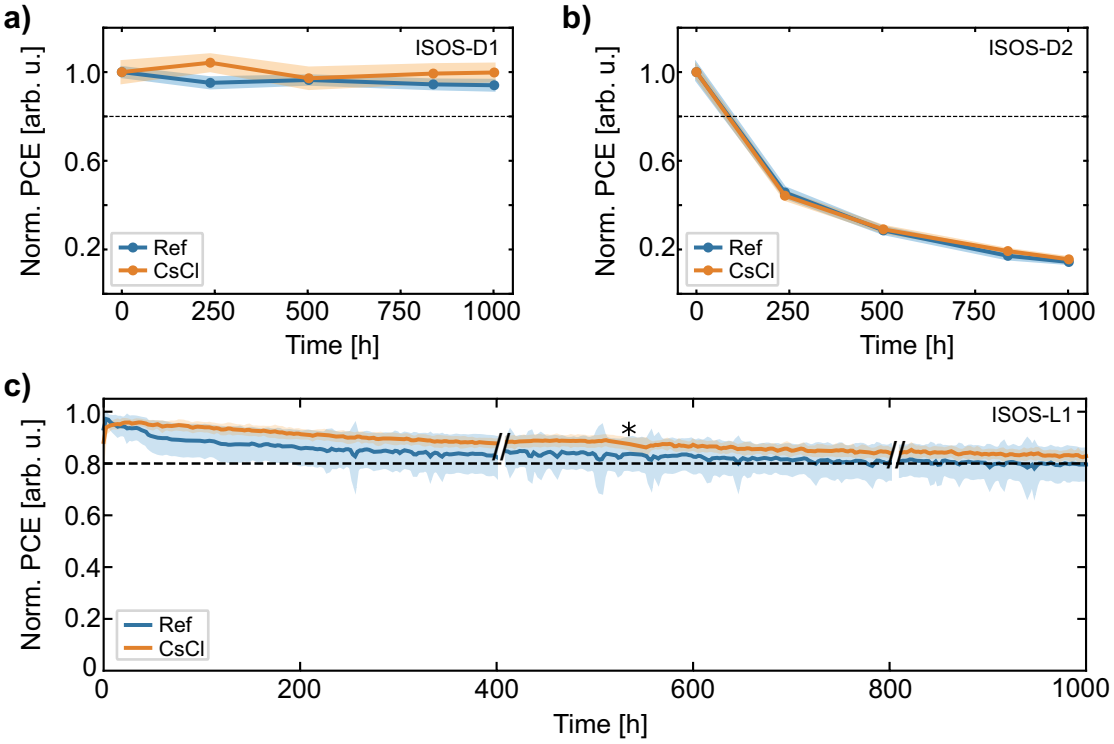

Figure 4: Normalized power conversion efficiency (PCE) from J–V measurements of semitransparent perovskite solar cells (PSCs) without any further modification (Ref) and with 5 nm CsCl seed layer (CsCl) under a) ISOS-D1 testing conditions (dark, intermittent J–V), and under b) ISOS-D2 testing conditions (dark, 85 °C, intermittent J–V) for 1000 h. Mean values and standard deviations based on twelve devices per parameter are provided. c) Normalized PCE at the maximum power point (MPP) tracking of semitransparent Ref and CsCl PSCs under ISOS-L1 test conditions (100 mW/cm^2, 25 °C, MPP tracking) for 1000 h. Mean values and standard deviations based on 10-14 devices per parameter are provided. // indicates brief periods when the solar simulator lamp was turned off, while * marks a short interruption in the measurement. To account for these pauses, the measurement duration was extended, ensuring a total exposure time of 1000 h.

In summary, the degradation mechanisms observed under various stress conditions reveal that devices with CsCl seed layer exhibit an improved long-term stability, particularly under dark storage and light exposure. Significant degradation at elevated temperatures highlights the need for further optimization.

2.4 2T Tandem Devices

Building on the successful implementation of the CsCl seed layer in single-junction PSCs, the strategy is extended to Si bottom cells for the fabrication of 2T perovskite/Si TSCs. The 2T perovskite/Si TSC architecture consists of the layer stack Si/ITO/NiO_x/2PACz/(CsCl)/perovskite/$PDAI_2$+BAI/C_{60}/SnO_x/IZO/Ag/MgF_2 with an active area of 1.0 cm^2. The compatibility of the fully solution-based two-step deposition method with textured Si surfaces has been demonstrated previously,[21] although large industrial textures (≈ 2-5 µm) increase the risk of incomplete coverage and shunting, which can severely impact fabrication yield. The thin CsCl seed layer is therefore investigated as a strategy to improve perovskite coverage and process reliability.

For small-textured Si bottom cells (0.5-1 µm pyramid height), a cross-sectional SEM image reveals that the inorganic scaffold can fully cover the pyramidal structure (Figure S13a). Top-view SEM images show a comparable porous morphology for both Ref and CsCl inorganic scaffolds, consistent with observations on glass substrates (Figure S13b/c). GIWAXS measurements confirm that inorganic scaffold formation is not affected by the substrate morphology (Figure S14a/b). After perovskite conversion, both Ref and CsCl perovskite films form a homogeneous layer with complete coverage of the surface texture (Figure 5a/b). Top-view SEM images show increased grain sizes compared to the inorganic scaffolds on glass substrates, with a slight enlargement for CsCl perovskite films (Figure S13d/e and Figure S15). GIWAXS analysis further reveals a reorientation of the (100) perovskite phase toward lower in-plane scattering angles compared to perovskite films on planar substrates, indicating a tendency toward more horizontally oriented crystal growth on textured surfaces (Figure S14c/d).

In contrast, for large-textured Si bottom cells (2-5 µm pyramid height), SEM images show incomplete coverage of the inorganic scaffold for both configurations, with partially exposed pyramid tips (Figure S16a-d). However, the introduction of a CsCl seed layer promotes a thin coating over the pyramidal tips, effectively acting as an insulating (wide-bandgap) interlayer that reduces shunt currents and improves coverage. Supplementary GIWAXS measurements indicate that the overall inorganic scaffold structure remains largely unaffected by the substrate texture (Figure S17a/b). After perovskite conversion, Ref perovskite films exhibit persistent uncovered regions, whereas the CsCl seed layer strategy improves perovskite film coverage with reduced exposed pyramidal tips (Figure 5c/d). Despite these differences in coverage, grain sizes remain comparable (Figure S18), and GIWAXS measurements show a similar texture-induced crystal reorientation as observed for small-textured substrates (Figure S17c/d).

Finally, 2T perovskite/Si TSCs are fabricated. A statistical analysis across two fabrication batches – six TSCs per bottom cell type and parameter in total (three TSCs per batch) – demonstrates that introducing a CsCl seed layer substantially improves the fabrication yield of 2T perovskite/Si TSCs (Figure 5e and Table S6/S7/S8). For planar Si bottom cells, the fabrication yield increases from 66% (Ref) to 83% (CsCl). The effect is even more pronounced for textured substrates, with fabrication yields increasing from 16% to 71% for small-textured Si bottom cells, and from 50% to 100% for large-textured Si bottom cells. This significant improvement highlights the effectiveness of the CsCl seed layer strategy at the HTL/perovskite interface in mitigating shunt formation and enabling reliable device fabrication, particularly on challenging textured surfaces.

High fabrication yield is a critical requirement for industrial PV manufacturing, where production yields typically need to exceed ∼95-98% to ensure economic viability.[43] Against this background, the observed yield improvements represent a significant step toward the scalable integration of 2T perovskite/Si TSCs, although further optimization is still required to reach industrial benchmarks.

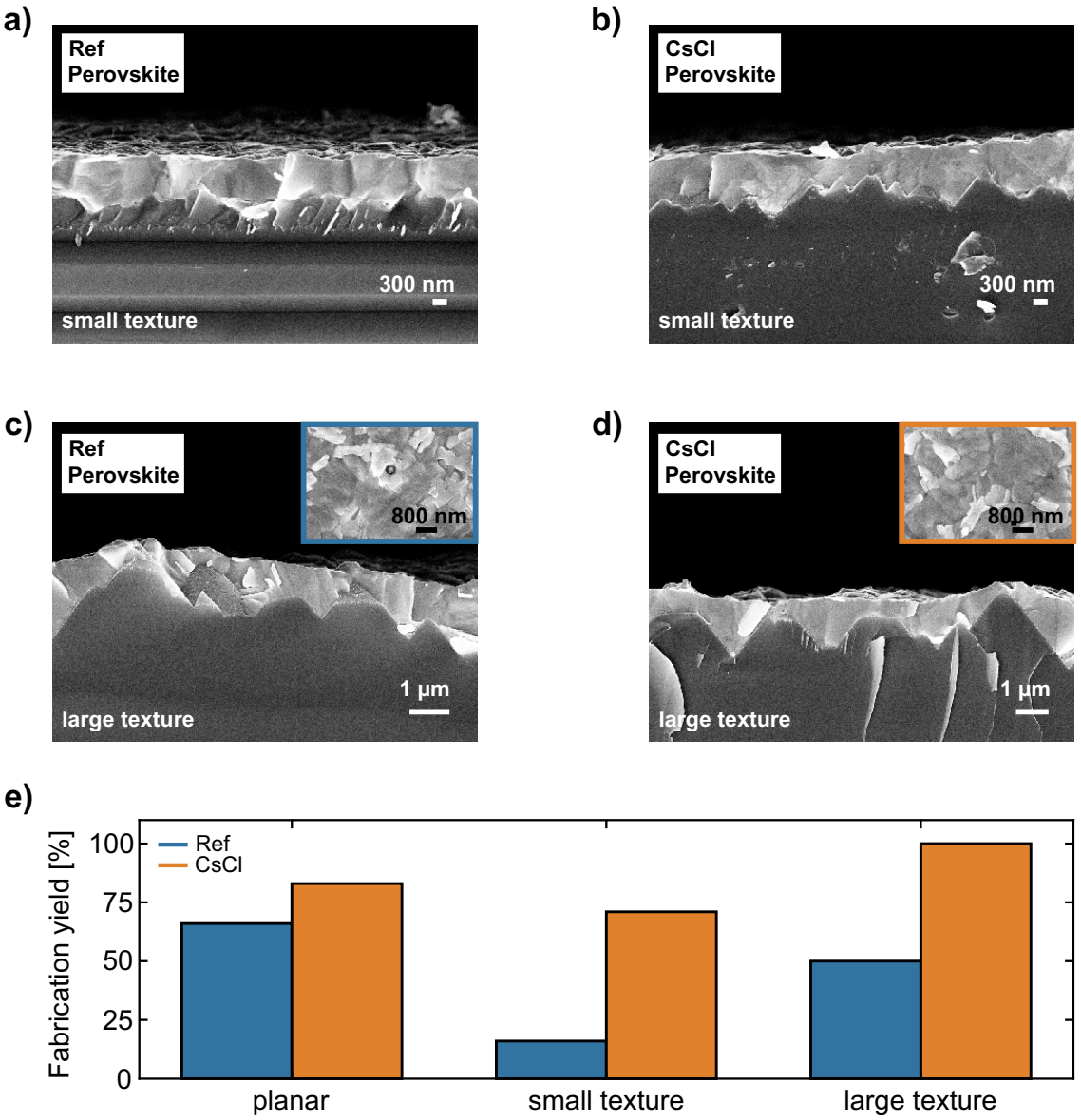

Figure 5: Representative cross-sectional scanning electron microscopy (SEM) images of perovskite films a) without any further modification (Ref) and b) with 5 nm CsCl seed layer (CsCl) deposited on small-textured (0.5-1 µm) Si bottom cells. Representative cross-sectional SEM images of large-textured (2-5 µm) Si bottom cells for c) Ref and d) CsCl perovskite films. Insets in c) and d) show corresponding top-view SEM images. The perovskite films are without surface passivation. e) Fabrication yield of 2T perovskite/Si tandem solar cells (TSCs) on planar, small-textured, and large-textured Si bottom cells. The fabrication yield is evaluated over two fabrication batches comprising six cells per bottom cell type and parameter. Only functional (not shunted) 2T perovskite/Si TSCs are accounted for.

3 Conclusion

This work demonstrates that introducing a thin CsCl seed layer at the HTL/perovskite interface provides a simple and highly effective strategy to enhance fabrication yield, device performance and stability of PSCs and 2T perovskite/Si TSCs in a solution-based two-step deposition method. While the CsCl seed layer induces only minor changes in film morphology and crystallization, it results in a significant improvement in FF and reduced hysteresis, achieving a champion PCE of 19.0% for a 1.67 eV bandgap single-junction PSC. In addition, CsCl seed layer devices exhibit enhanced operational long-term stability, re-

taining 84% of their initial device performance after 1000 h of continuous illumination. When transferred to 2T perovskite/Si TSCs, the CsCl seed layer proves particularly beneficial for textured Si bottom cells. By improving perovskite coverage and reducing shunting on submicron- and micron-scale textures, the strategy substantially increases fabrication yield without requiring modifications to the established processing route. This compatibility with industrially relevant surface textures highlights the potential of the strategy for industrially relevant tandem device fabrication. Beyond the specific system studied here, these results establish a broader design principle: ultrathin seed layers can effectively modulate nucleation and thin-film formation in solution-processed perovskites, bridging the gap between solution-based and hybrid deposition methods. As such, CsCl seed layers represent a practical pathway to improve fabrication yield, device performance, and long-term operational stability in PSCs while enabling their successful integration into textured tandem architectures.

4 Experimental Section

Materials

2PACz (TCI, CAS: 20999-38-6), Lead iodide (PbI_2: TCI, CAS: 10101-63-0), Lead bromide ($PbBr_2$: TCI, CAS: 10031-22-8), Formamidinium iodide (FAI: Greatcell solar materials, CAS: 879643-71-7), Formamidinium bromide (FABr: Dyenamo, CAS: 146958-06-7), Methylammonium chloride (MACl: Dyenamo, CAS: 593-51-1), Cesium iodide (CsI: TCI, CAS: 7647-17-8), Cesium chloride (CsCl: TCI, CAS: 7647-17-8), Fullerene-C_{60} (C_{60}: Sigma-Aldrich, CAS: 99685-96-8), n-Butylammonium iodide (BAI: Greatcell solar materials, CAS: 36945-08-1), Propane-1,3-diammonium iodide ($PDAI_2$: Greatcell solar materials, CAS: 120675-53-8). All solvents including N,N-dimethylformamide, 99.8% (DMF, CAS: 68-12-2), Dimethyl sulfoxide anhydrous, $\geq$ 99.9% (DMSO, CAS: 67-68-5), 2-Propanol, 99.5%, (IPA, CAS: 67-63-0) and Ethanol absolute anhydrous, $\geq$ 99.8%, (EtOH, CAS: 64-17-5) were ordered from VWR Chemicals.

Device Fabrication

Single-Junction (SJ) Perovskite Solar Cells

The planar *p-i-n* PSCs with the layer stack glass/ITO/NiO_x/2PACz/perovskite/$PDAI_2$+BAI/C_{60}/SnO_2/Ag were fabricated as follows.

Substrates and HTL: The glass substrates with 120 nm thick indium tin oxide (ITO) coating (sheet resistance 15 Ωcm^{-2}, Luminescence Technology, CAS: 50926-11-9) were cut in 16 mm $\times$ 16 mm and cleaned in an ultrasonic bath with deionized (DI) water with glass cleaner, acetone and IPA for 10 min each. This is followed by 3 min of oxygen plasma treatment before the deposition of the hole transport (HTL) layer. For the HTL layer, a 5 nm thick NiO_x film was sputtered from a NiO_x target (4 inch, 99.99% pure, Kurt J. Lesker Company) using 100 W power (7.95 W in^{-2} power density) in a gas mixture of Ar and O_2 at 1 mTorr on the ITO substrate with a fixed flow rate of 0.2 sccm for O_2 and a variable flow rate of Ar to achieve the set pressure. Then, a thin layer of 2PACz was deposited on the ITO/NiO_x substrate by spin-coating at 3000 rpm for 30 s and subsequently annealed at 100 °C for 10 min. For the samples with CsCl seed layer, a washing step was used to remove any unbound molecules. Here, 150 µL of pure EtOH was used which was dynamically dispensed onto the substrate within 5 s at 3000 rpm for 30 s of total rotation time. The substrates were then annealed at 100 °C for 10 minutes. The 2PACz precursor solution was prepared by dissolving 2PACz in anhydrous EtOH with a concentration of 0.375 mg mL^{-1}. The prepared solution was placed in an ultrasonic bath for at least 20 min before use.

Perovskite solution: For the samples with CsCl seed layer, physical vapor deposition of CsCl was performed in a PEROvap system (M.Braun Inertgas-Systeme GmbH Dresden) integrated into a N_2-filled glovebox. A cooling inner surface, surrounding all sublimation sources, was set to −20 °C. Prior to the heating process, the system was evacuated, with a standard base pressure at start of heating of $< 3x10^{-6}$ mbar mbar. The substrate temperature (18 °C) was kept constant for all experiments. Source to substrate setup uses a 300 mm vertical distance and 165 mm lateral distance between the sublimation source and the substrate. The final thickness of CsCl was 5 nm with a static deposition rate of 0.1 Å s^{-1}. For all experiments, cylindrical 10 cm^3 crucibles were used with material filling of $\approx$ 5 g for CsCl.

The double-cation perovskite ($Cs_{0.16}FA_{0.84}Pb(I_{0.79}Br_{0.21})_3$) solution was prepared according to our previous work[21]. Two different solutions were prepared. For the inorganic solution, 1.275 M PbI_2 and 0.225 M $PbBr_2$ were dissolved in 1 mL DMF:DMSO (9:1

volume ratio, v:v; less DMSO, since it was added with the CsI solution) and heated up to 130 °C for 30 min to completely dissolve the materials. After cooling down, 70 µL CsI solution (corresponds to 7 mol% CsI, 390 mg mL^{-1} CsI in DMSO) was added to the inorganic solution. The organic cation solution was prepared by dissolving FAI (58.5 mg), FABr (27.9 mg) and MACl (9 mg) in 1 mL IPA. The addition of MACl improves the crystallization of the perovskite film but evaporates in the final annealing step.[44] For bulk passivation, a bimolecular passivation containing 0.1 mg mL^{-1} $PDAI_2$ and 0.1 mg mL^{-1} BAI dissolved in IPA was added to the organic cation solution.

Perovskite film fabrication: All perovskite absorber layers were deposited on the substrate using the solution-based two-step deposition method. The first step was the deposition of the inorganic PbI_2 layer. This was achieved by dropping 60 µL of the inorganic solution and spin-coating at 1500 rpm for 30 s. The films were subsequently annealed at 70 °C for 1 min resulting in a yellow-transparent layer. The formation of the perovskite was achieved by dropping 80 µL of the cation solution on top of the inorganic scaffold and rapidly starting the spin-coating process at 2500 rpm for 30 s, which resulted in a red film. This was followed by an annealing step at 150 °C for 15 min outside of the glovebox under ambient conditions (at a relative humidity of 20-50%) converting it to the desired black perovskite film. It has to be noted that the spin-coating process took place in a N_2-filled glovebox. For the second annealing step, a transport-box was used to transfer the samples out of the glovebox in order to keep the samples in a nitrogen atmosphere right before the annealing on a preheated plate (150 °C). As soon as the transport-box was opened, the crystallization and phase-change process started and a rapid transfer to the hotplate directly after opening the transport-box was beneficial for the cell performance.[45] After annealing, 100 µL of a bimolecular passivation containing 1.25 mg mL^{-1} $PDAI_2$ and 1.25 mg mL^{-1} BAI dissolved in IPA was dynamically spin-coated on the perovskite films at 4500 rpm for 30 s, followed by annealing at 100 °C for 5 min.

ETL and Top Contact: As electron transport (ETL) layer, 20 nm of C_{60} were thermally evaporated and deposited using an Angstrom evaporation system at an evaporation rate of 0.1 - 0.2 Å s^{-1} at a pressure of around 10^{-6} mbar. A 20 nm SnO_2 layer prepared by atomic layer deposition (ALD) was used as buffer layer. Subsequently, 100 nm Ag was thermally evaporated using a shadow mask to define the active area to 10.5 mm^2 and complete the PSCs with 4 pixels per substrate. For measuring with the solar simulator, a shadow mask with an area of 7.84 mm^2 was used.
For stability measurements, semitransparent devices with the layer stack glass/ITO/ NiO_x/2PACz/perovskite/surface passivation/C_{60}/SnO_x/IZO/Au were prepared. The 20 nm SnO_2 layer is followed by 90 nm sputtered indium zinc oxide (IZO) and 75 nm thermally evaporated Au (using a shadow mask). For measuring with the solar simulator, a shadow mask with an area of 7.84 mm^2 was used.

2T Perovskite/Silicon Tandem Devices

Before depositing the HTL layer, the silicon cells were cleaned with acetone and IPA in a spin-coater process. For the HTL layer, a 15 nm thick NiO_x film was sputtered from a NiO_x target (4 inch, 99.99% pure, Kurt J. Lesker Company) using 100 W power (7.95 W in^{-2} power density) in a gas mixture of Ar and O_2 at 1 mTorr on the silicon bottom cell with ITO layer with a fixed flow rate of 0.2 sccm for O_2 and a variable flow rate of Ar to achieve the set pressure. This was followed by a thin 2PACz layer deposited as mentioned above with a higher concentrated 2PACz solution with 0.475 mg mL^{-1}. For the samples with CsCl seed layer, a washing step was used to remove any unbound molecules and 5 nm CsCl were vapor-deposited as described before. The perovskite absorber layer was fabricated as previously described, using higher concentrated solutions of 1.7 M for small textures and 1.9 M for large textures. Bulk passivation followed the same approach as for

SJ cells but was adjusted to match the perovskite solution molarity. For small textures, the concentration of the surface passivation was the same as in SJ cells. For large textures, the concentration was reduced to 0.3 mg mL^{-1} for $PDAI_2$ and 0.3 mg mL^{-1} for BAI. For the ETL layer, 20 nm of C_{60} was thermally evaporated at an evaporation rate of 0.1 - 0.2 Å $^{-1}$ at a pressure of around 10^{-6} mbar. A 20 nm SnO_2 layer prepared by atomic layer deposition (ALD) was used as buffer layer. Subsequently, 45 nm sputtered IZO was used as a transparent electrode and the active area of 1.04 cm^2 was defined by the thermally evaporated Ag electrode (600 nm with 3x150 µm gridfingers). In order to reduce the reflection losses, 100 nm MgF_2 as an antireflection layer was evaporated on top of the Ag. For measuring with the solar simulator, a shadow mask with an area of 1.0 cm^2 was used.

Device Characterization

Current Density-Voltage (*J*–*V*) Measurements

The *J*–*V* characteristics of the SJ PSCs were measured with a class AAA xenon-lamp solar simulator (Newport Oriel Sol3A) with a scan rate set at 0.6 V s^{-1} using a sourcemeter (Keithley 2400) with an air-mass 1.5 global (AM1.5G) spectra (100 mW cm^{-2}, Figure S19). The solar simulator irradiation intensity was calibrated using a certified silicon solar cell (Fraunhofer ISE, calibrated 2024) equipped with a KG5 band pass filter (Schott). The maximum power point (MPP) tracking was performed under a class AAA LED-based solar simulator (Wavelabs, LS-2), while the temperature of the devices was controlled at 25 °C. The spectrum was a close match to that of AM1.5G over the relevant spectral range (98 mW cm^{-2}). The measurement was performed in a N_2-filled glovebox.
The *J*–*V* characteristics of the perovskite/Si TSCs were measured with a class AAA LED-based solar simulator (Wavelabs, LS-2) with a scan rate set at 0.6 V $^{-1}$ using a sourcemeter (Keithley 2400) with an air-mass 1.5 global (AM1.5G) spectra (100 mW cm^{-2}). The solar simulator irradiation intensity was calibrated using a certified silicon solar cell (Fraunhofer ISE). The measurement was performed in ambient atmosphere.

External Quantum Efficiency (EQE) Measurements

The EQE was measured using a PVE300 photovoltaic QE system (Bentham EQE system). A chopping frequency in the range of 560 - 590 Hz with an integration time of 500 ms (750 ms for 2T tandems) to acquire the spectra in a wavelength range from 300 to 850 nm (300 to 1200 nm for 2T tandems) was used. An illumination spot (0.74 mm for SJ, 2.0 mm^2 for 2T tandems) was utilized to obtain the average over possible variations in the EQE spectra. The bandgap of all processed perovskite thin films is determined based on the differential of the EQE curves near the absorption edge (maximum of d(EQE)/d(E)) according to Krückemeier *et al.*[46].

Scanning Electron Microscopy (SEM)

SEM analyses were carried out in a scanning electron microscope (Zeiss LEO1530) with an in-lens detector and a aperture size of 20 - 30 µm. For cross-sectional analyses, the cross sections were covered with a 3 nm thick platinum layer deposited by sputtering to prevent charging. The applied acceleration voltages for surface and cross sectional analyses range between 5 and 10 kV.

Atomic Force Microscopy (AFM)

AFM images were obtained using a Nano Wizard II (JPK Instruments). The scanning area was 5 µm × 5 µm. For each parameter, 2 - 3 measurements were conducted, and the average root-mean-square (RMS) value was determined.

UV-Vis Spectrophotometry (UV)

Transmittance and reflectance spectra of the perovskite thin films were measured using a PerkinElmer Lambda1050 spectrophotometry setup equipped with a double-monochromator and a modulated source. A chopper frequency of 46 Hz was applied.

X-Ray Diffraction (XRD)

The crystal structure of the perovskite layers was carried out utilizing XRD (Bruker D2 Phaser system) with Cu-K_α radiation (λ = 1.5405 Å) in Bragg-Brentano configuration using a LynxEye detector. The XRD was taken from the perovskite layer deposited on the ITO/NiO_x/2PACz substrate to obtain the same perovskite nucleation as well as crystallization as in the solar cells. The crystallite size D depending on the FWHM can be calculated according to the Scherrer equation

$$D = \frac{K\lambda}{\beta \cos(\Theta)}, \tag{1}$$

where K a constant, λ the X-ray wavelength, β the FWHM and Θ the diffraction angle.[47,48]

Grazing-Incidence Wide-Angle X-Ray Scattering (GIWAXS)

The GIWAXS measurements were carried out on a Bruker D8 Advance equipped with a Cu X-ray source (40 kV, 40 mA), a Goebel mirror, a 0.5 mm micro mask and a 0.3 mm snout on the primary track and an Eiger2 R 500K 2D detector on the secondary track. The incidence angle was fixed at 1.5°. First, all acquired images were projected onto a virtual detector directly behind the real goniometer circle using a home-developed program in MATLAB.[49] For reshaping the experimentally acquired data into 2D diffractograms in reciprocal space, the open-access software GIXSGUI was used.[50]

Time-of-Flight Secondary Ion Mass Spectrometry (ToF-SIMS)

Time-of-Flight Secondary Ion Mass Spectrometry, (ToF-SIMS), was performed on a TOF.SIMS5 instrument (ION-TOF GmbH, Münster, Germany) equipped with a Bi cluster primary ion source and a reflectron type time-of-flight analyzer. Ultra-high vacuum (UHV) base pressure during analysis was $< 7\times10^{-8}$ mbar. For high mass resolution the Bi source was operated in the "high current bunched" mode providing short Bi_3^+ primary ion pulses at 25 keV energy, a lateral resolution of approx. 4 µm, and a target current of 0.1 pA. The short pulse length of 1.5 ns allowed for high mass resolution (6500 m/Δm for $^{208}Pb^+$). The primary ion beam was rastered across a 100×100 µm^2 field of view on the sample, and 64×64 data points were recorded. Mass scale calibrations were based on ^{12}C, $^{12}C_2$, ^{35}Cl, InO, I_2, respectively. For depth profiling, a dual beam analysis in non-interlaced mode (2 s sputter, 1 s pause, charge compensation) was performed. For negative secondary ion polarity, the sputter gun for depth profiling was operated with O_2^+ ions, 1 keV, scanned over a concentric field of 250×250 µm^2 (target current 257 nA). The applied sputter ion fluence was used as an arbitrary measure for depth. Note, however, that this scale might not be linear due to different erosion speeds of the different deposited layers. Secondary ion intensities are plotted normalized to their maximum intensities each, yielding higher noise levels for weaker absolute intensities. It was ensured that signals showing SI detector saturation were omitted.

Photoluminescence Quantum Yield (PLQY)

PLQY measurements were carried out using a LuQY Pro setup from QYB. The samples were mounted inside an integrating sphere in ambient air and a green laser (λ = 532

nm) was directed into the sphere via a small entrance port. The radiative limit of the V_{OC} ($V_{\mathrm{OC-rad}}$) and the implied V_{OC} ($V_{\mathrm{OC-imp}}$) were determined from the (intensity-dependent) PLQY measurements as described by Stolterfoht *et al.*[51] and Kirchartz *et al.*[46] From the quasi-Fermi level splitting (QFLS, E_F) one can calculate the 'implied V_{OC}' *via*

$$V_{OC-imp} = \frac{\Delta E_F}{q} = V_{OC-rad} + \frac{k_B T}{q} \ln\left(PLQY \frac{J_G}{J_{0-rad}} \right), \tag{2}$$

where V_{OC-rad} is the radiative limit, k_B the Boltzmann constant, T the temperature, q the elemental charge, J_G the generation current density and J_{0-rad} the radiative thermal recombination current density in the dark. The internal ideality factor ($\mathrm{n_{id}}$) was determined from these measurements as a fit to the calculated $V_{\mathrm{OC-imp}}$.[51,52]

Statistical Analysis

To check the deviation of the statistical results from each other, *Welch's t test* was applied. *Welch's t test* is an adaption of the *Student's t* test[36] and is more reliable when the two samples have unequal variances and possibly unequal sample sizes.[53,54] These tests are often referred to as "independent samples" or "unpaired" t tests because they are usually applied when the statistics underlying the two samples being compared do not overlap. It is assumed that the sample means for the two samples being compared are normally distributed.[36]

The t statistic for testing whether the results differ from each other or not can be calculated as follows:

$$t = \frac{\overline{X} - \overline{Y}}{\sqrt{\frac{S_x^2}{n_x} + \frac{S_y^2}{n_y}}}, \tag{3}$$

whereas $\overline{X}$ and $\overline{Y}$ are the mean values, S_x and S_y the standard deviations and n_x and n_y the sample sizes.

PSCs with a V_{OC} below 0.8 V and a FF below 60% were excluded to filter out statistically irrelevant data.

Acknowledgements

This work was partly carried out with the support of the Karlsruhe Nano Micro Facility (KNMFi, www.knmf.kit.edu), an Open Access Research Infrastructure within the Karlsruhe High Technology Hub at the Karlsruhe Institute of Technology (KIT – The University in the Helmholtz Association, www.kit.edu). Financial support by the Initiating and Networking funding of the Helmholtz Association (Project Zeitenwende and the Solar Technology Acceleration Platform (Solar TAP)), by the Ministry of Science and Culture in the State of Lower Saxony through the program "zukunft.niedersachsen" (project NextGenPV), by the program oriented funding IV of the Helmholtz Association (Materials and Technologies for the Energy Transition, Topic 1: Photovoltaics and Wind Energy, Code: 38.01.03), and the German Federal Ministry for Economic Affairs and Energy (BMWE) through the SHAPE project (03EE1123 A-E) and the HYPER project (03EE1222B) is greatly acknowledged. We acknowledge support by the Karlsruhe School of Optics & Photonics (KSOP) and the Ministry of Science, Research and Arts of Baden-Württemberg as part of the sustainability financing of the projects of the Excellence Initiative II. This work was partially funded by the European Union. Views and opinions expressed are however those of the author(s) only and do not necessarily reflect those of the European Union or RIA. Neither the European Union nor the granting authority can be held responsible for them. The NEXUS project has received funding from the European Union's Horizon Europe research and innovation program under grant agreement No. 101075330. The authors thank the whole "Perovskite Taskforce" at KIT for fruitful discussions and assistance.

Authors Contribution

Ronja Pappenberger: Conceptualization, Formal analysis, Investigation (Lead), Data Curation (Lead), Writing - Original Draft, Visualization, Project administration. **Alexander Diercks:** Investigation (SEM), Writing - Review & Editing. **Roja Singh:** Investigation (Stability), Writing - Review & Editing. **Alexander Welle:** Investigation (ToF-SIMS), Data Curation (Supporting), Writing - Review & Editing. **Tonghan Zhao:** Investigation (GIWAXS), Data Curation (Supporting), Writing - Review & Editing. **Julian Petry:** Conceptualization (Supporting), Writing - Review & Editing. **Ulrich W. Paetzold:** Conceptualization (Supporting), Writing - Review & Editing, Supervision, Funding acquisition.

Conflict of Interest

The authors declare no conflict of interest.

Data Availability Statement

The data supporting this article has been included as part of the ESI. The data generated during and/or analyzed during the current study has been deposited at the KITopen repository under a CC-BY 4.0 Creative Commons Attribution license: KITopen (2026), **DOI will be added upon acceptance**.

References

[1] A. Kojima, K. Teshima, Y. Shirai, and T. Miyasaka. Organometal halide perovskites as visible-light sensitizers for photovoltaic cells. *Journal of the American Chemical Society*, 131(17):6050–6051, 2009.

[2] National Laboratory of the Rockies (NLR). Best Research-Cell Efficiency Chart. `https://www.nlr.gov/pv/cell-efficiency.html`. accessed: May, 2026.

[3] T. Niewelt, B. Steinhauser, A. Richter, B. Veith-Wolf, A. Fell, B. Hammann, N.E. Grant, L. Black, J. Tan, A. Youssef, J.D. Murphy, J. Schmidt, M.C. Schubert, and S.W. Glunz. Reassessment of the intrinsic bulk recombination in crystalline silicon. *Sol. Energy Mater. Sol. Cells*, 235:111467, 2022.

[4] F. E. Subhan, A. D. Khan, A. D. Khan, N. Ullah, M. Imran, and M. Noman. Optical optimization of double-side-textured monolithic perovskite-silicon tandem solar cells for improved light management. *RSC Advances*, 10(45):26631–26638, 2020.

[5] M. De Bastiani, Alessandro J. Mirabelli, Y. Hou, F. Gota, E. Aydin, T. G. Allen, J. Troughton, A. S. Subbiah, F. H. Isikgor, J. Liu, L. Xu, B. Chen, E. Van Kerschaver, D. Baran, B. Fraboni, M. F. Salvador, U. W. Paetzold, E. H. Sargent, and S. De Wolf. Efficient bifacial monolithic perovskite/silicon tandem solar cells via bandgap engineering. *Nature Energy*, 6(2):167–175, 2021.

[6] F. Gota, R. Schmager, A. Farag, and U. W. Paetzold. Energy yield modelling of textured perovskite/silicon tandem photovoltaics with thick perovskite top cells. *Optics Express*, 30(9):14172, 2022.

[7] W. Qarony, M. I. Hossain, V. Jovanov, A. Salleo, D. Knipp, and Y. H. Tsang. Influence of perovskite interface morphology on the photon management in perovskite/silicon tandem solar cells. *ACS Applied Materials & Interfaces*, 12(13):15080–15086, 2020.

[8] A. S. Subbiah, F. H. Isikgor, C. T. Howells, M. De Bastiani, J. Liu, E. Aydin, F. Furlan, T. G. Allen, F. Xu, S. Zhumagali, S. Hoogland, E. H. Sargent, I. McCulloch, and S. De Wolf. High-performance perovskite single-junction and textured perovskite/silicon tandem solar cells via slot-die-coating. *ACS Energy Letters*, 5(9):3034–3040, 2020.

[9] F. H. Isikgor, F. Furlan, J. Liu, E. Ugur, M. K. Eswaran, A. S. Subbiah, E. Yengel, M. De Bastiani, G. T. Harrison, S. Zhumagali, C. T. Howells, E. Aydin, M. Wang, N. Gasparini, T. G. Allen, A. ur Rehman, E. Van Kerschaver, D. Baran, I. McCulloch, T. D. Anthopoulos, U. Schwingenschlögl, F. Laquai, and S. De Wolf. Concurrent cationic and anionic perovskite defect passivation enables 27.4% perovskite/silicon tandems with suppression of halide segregation. *Joule*, 5(6):1566–1586, 2021.

[10] F. Sahli, J. Werner, B.t A. Kamino, M. Bräuninger, R. Monnard, B. Paviet-Salomon, L. Barraud, L. Ding, J. J. Diaz-Leon, D. Sacchetto, G. Cattaneo, M. Despeisse, M. Boccard, S. Nicolay, Q. Jeangros, B. Niesen, and Chr. Ballif. Fully textured monolithic perovskite/silicon tandem solar cells with 25.2% power conversion efficiency. *Nature Materials*, 17(9):820–826, 2018.

[11] M. Jošt, T. Bertram, D. Koushik, J. A. Marquez, M. A. Verheijen, M. D. Heinemann, E. Köhnen, A. Al-Ashouri, S. Braunger, F. Lang, B. Rech, T. Unold, M. Creatore, I. Lauermann, C. A. Kaufmann, R. Schlatmann, and S. Albrecht. 21.6%-efficient monolithic perovskite/Cu(In,Ga)Se_2 tandem solar cells with thin conformal hole transport layers for integration on rough bottom cell surfaces. *ACS Energy Letters*, 4(2):583–590, 2019.

[12] L. Cojocaru, K. Wienands, T. W. Kim, S. Uchida, A. J. Bett, S. Rafizadeh, J. C. Goldschmidt, and S. W. Glunz. Detailed investigation of evaporated perovskite absorbers with high crystal quality on different substrates. *ACS Applied Materials & Interfaces*, 10(31):26293–26302, 2018.

[13] M. Roß, S. Severin, M. B. Stutz, P. Wagner, H. Köbler, M. Favin-Lévêque, A. Al-Ashouri, P. Korb, P. Tockhorn, A. Abate, B. Stannowski, B. Rech, and S. Albrecht. Co-evaporated formamidinium lead iodide based perovskites with 1000 h constant stability for fully textured monolithic perovskite/silicon tandem solar cells. *Advanced Energy Materials*, 11(35), 2021.

[14] Martin Kroll, Seren Dilara Öz, Zongbao Zhang, Ran Ji, Tim Schramm, Tobias Antrack, Yana Vaynzof, Selina Olthof, and Karl Leo. Insights into the evaporation behaviour of fai: material degradation and consequences for perovskite solar cells. *Sustainable Energy Fuels*, 6:3230–3239, 2022.

[15] Juliane Borchert, Ievgen Levchuk, Lavina C. Snoek, Mathias Uller Rothmann, Renée Haver, Henry J. Snaith, Christoph J. Brabec, Laura M. Herz, and Michael B. Johnston. Impurity tracking enables enhanced control and reproducibility of hybrid perovskite vapor deposition. *ACS Applied Materials & Interfaces*, 11(32):28851–28857, 2019. PMID: 31314481.

[16] Ievgen Levchuk, Yi Hou, Marco Gruber, Marco Brandl, Patrick Herre, Xiaofeng Tang, Florian Hoegl, Miroslaw Batentschuk, Andres Osvet, Rainer Hock, Wolfgang Peukert, Rik R. Tykwinski, and Christoph J. Brabec. Deciphering the role of impurities in methylammonium iodide and their impact on the performance of perovskite solar cells. *Advanced Materials Interfaces*, 3(22):1600593, 2016.

[17] Kassio P. S. Zanoni, Lucia Martínez-Goyeneche, Chris Dreessen, Michele Sessolo, and Henk J. Bolink. Photovoltaic devices using sublimed methylammonium lead iodide perovskites: Long-term reproducible processing. *Solar RRL*, 7(7):2201073, 2023.

[18] B. Chen, P. Wang, R. Li, N. Ren, W. Han, Z. Zhu, J. Wang, S. Wang, B. Shi, J. Liu, P. Liu, Q. Huang, S. Xu, Y. Zhao, and X. Zhang. A two-step solution-processed wide-bandgap perovskite for monolithic silicon-based tandem solar cells with $> 27\%$ efficiency. *ACS Energy Letters*, 7(8):2771–2780, 2022.

[19] Q. Li, Y. Zhao, W. Zhou, Z. Han, R. Fu, F. Lin, D. Yu, and Q. Zhao. Halogen engineering for operationally stable perovskite solar cells via sequential deposition. *Advanced Energy Materials*, 9(46):1902239, 2019.

[20] R. Pappenberger, A. Diercks, J. Petry, S. Moghadamzadeh, P. Fassl, and U. W. Paetzold. Bandgap engineering of two-step processed perovskite top cells for perovskite-based tandem photovoltaics. *Advanced Functional Materials*, 34(9), 2023.

[21] R. Pappenberger, R. Singh, A. Diercks, T. Zhao, R. Pesch, J. Petry, D. Baumann, X. Liu, and U. W. Paetzold. Versatile two-step process for perovskite-based tandem photovoltaics. *Solar RRL*, 9(13), 2025.

[22] A. Diercks, J. Petry, T. Feeney, R. Singh, T. Zhao, H. Hu, Y. Li, U. W. Paetzold, and P. Fassl. Sequential evaporation of inverted $FAPbI_3$ perovskite solar cells – impact of substrate on crystallization and film formation. *ACS Energy Letters*, 10(3):1165–1173, 2025.

[23] K. Geistert, R. Pappenberger, P. Scharfer, P. Cavadini, W. Schabel, F. Sadegh, D. B. Ritzer, B. Abdollahi Nejand, and U. W. Paetzold. Spatially regulated gas flow control for batch-drying of large area slot-die-coated perovskite thin films. *Advanced Energy Materials*, 2025.

[24] R. Pesch, A. Diercks, J. Petry, A. Welle, R. Pappenberger, F. Schackmar, H. Eggers, J. Sutter, U. Lemmer, and U. W. Paetzold. Hybrid two-step inkjet-printed perovskite solar cells. *Solar RRL*, 8(13), 2024.

[25] R. Pesch, J. Petry, J. Petermann, R. Pappenberger, T. Kuechle, J. Schenck, L. P. Rothbauer, L. Fang, X. Liu, S. Rafizadeh, B. A. Nejand, J. Sutter, U. Lemmer, and U. W. Paetzold. Efficient perovskite/silicon tandem solar cells using hybrid two-step inkjet printing with edge isolation precision. *Small Science*, 2025.

[26] P. S.C. Schulze, K. Wienands, A. J. Bett, S. Rafizadeh, L. E. Mundt, L. Cojocaru, M. Hermle, S. W. Glunz, H. Hillebrecht, and J. C. Goldschmidt. Perovskite hybrid evaporation/spin coating method: From band gap tuning to thin film deposition on textures. *Thin Solid Films*, 704:137970, 2020.

[27] Yucheng Li, Biao Shi, Qiaojing Xu, Lingling Yan, Ningyu Ren, Yongliang Chen, Wei Han, Qian Huang, Ying Zhao, and Xiaodan Zhang. Wide bandgap interface layer induced stabilized perovskite/silicon tandem solar cells with stability over ten thousand hours. *Advanced Energy Materials*, 11(48):2102046, 2021.

[28] Xin Luo, Haowen Luo, Hongjiang Li, Rui Xia, Xuntian Zheng, Zilong Huang, Zhou Liu, Han Gao, Xueling Zhang, Songlin Li, Zhiqiang Feng, Yifeng Chen, and Hairen Tan. Efficient perovskite/silicon tandem solar cells on industrially compatible textured silicon. *Advanced Materials*, 35(9):2207883, 2023.

[29] O. Er-raji, L. Rustam, B. P. Kore, S. W. Glunz, and P. S. C. Schulze. Insights into perovskite film formation using the hybrid evaporation/spin-coating route: An in situ xrd study. *ACS Applied Energy Materials*, 6(11):6183–6193, 2023.

[30] Oussama Er-raji, Mohamed A.A. Mahmoud, Oliver Fischer, Alexandra J. Ramadan, Dmitry Bogachuk, Alexander Reinholdt, Angelika Schmitt, Bhushan P. Kore, Thomas William Gries, Artem Musiienko, Oliver Schultz-Wittmann, Martin Bivour, Martin Hermle, Martin C. Schubert, Juliane Borchert, Stefan W. Glunz, and Patricia S.C. Schulze. Tailoring perovskite crystallization and interfacial passivation in efficient, fully textured perovskite silicon tandem solar cells. *Joule*, 8(10):2811–2833, 2024.

[31] J. Petry, R. Pappenberger, A. Welle, T. Zhao, A. Diercks, R. Pesch, M. Krause, P. Fassl, and U. W. Paetzold. Benchmarking inorganic deposition routes for hybrid two-step processed perovskite solar cells: A materials perspective. *Solar RRL*, 10(4), 2026.

[32] Q. Luo, M. Wu, H. Zhang, M. He, S. Wu, H. Tan, J. Yang, K. Sun, Z. Wang, H. Yang, and Y. Mai. Combined evaporation-solution methodology for high-efficiency perovskite solar cells with exceptional reproducibility. *Journal of Materials Chemistry A*, pages 25782–25789, 2025.

[33] V. Škorjanc, A. Miaskiewicz, M. Roß, S. Maniyarasu, S. Severin, M. R. Leyden, P. Holzhey, F. Ruske, L. Korte, and S. Albrecht. Seed layers for wide-band gap coevaporated perovskite solar cells: CsCl regulates band gap and reduces process variability. *ACS Energy Letters*, 9(11):5639–5646, 2024.

[34] V. Škorjanc, S. Severin, A. Veber, M. J. Prieto, L. C. Tănase, A. Miaskiewicz, Sebastian Weitz, J.-W. Hsueh, M.-A. Mawass, L. de Souza Caldas, S. Manyarasu, P. Holzhey, E. Wutke, S. Demchyshyn, M. R. Leyden, A. Harter, R. F. Duarte, J. Kurpiers, P. Wagner, B. Stannovski, L. Puskar, R. Mainz, D. Abou-Ras, T. Schmidt, L. Korte, M. Roß, and S. Albrecht. CsCl seed layer homogenizes co-evaporated perovskite growth for high-efficiency fully textured perovskite-silicon tandem solar cells. *arXiv*, 2025.

[35] Lin Mao, Tian Yang, Hao Zhang, Jianhua Shi, Yuchao Hu, Peng Zeng, Faming Li, Jue Gong, Xiaoyu Fang, Yinqing Sun, Xiaochun Liu, Junlin Du, Anjun Han, Liping Zhang, Wenzhu Liu, Fanying Meng, Xudong Cui, Zhengxin Liu, and Mingzhen Liu. Fully textured, production-line compatible monolithic perovskite/silicon tandem solar cells approaching 29% efficiency. *Advanced Materials*, 34(40):2206193, 2022.

[36] B. L. Welch. The generalization of 'student's' problem when several different population varlances are involved. *Biometrika*, 34(1-2):28–35, 1947.

[37] X. Liu, X. Jiang, Y. Yin, J. Zhang, H. Tian, J. Guo, X. Guo, and C. Li. Dominating (111) facets with ordered stacking in perovskite films. *Energy & Environmental Science*, 17(16):6058–6067, 2024.

[38] K. Meng, X. Wang, Q. Xu, Z. Li, Z. Liu, L. Wu, Y. Hu, N. Liu, and G. Chen. In situ observation of crystallization dynamics and grain orientation in sequential deposition of metal halide perovskites. *Advanced Functional Materials*, 29(35), 2019.

[39] M. V. Khenkin, E. A. Katz, A. Abate, G. Bardizza, J. J. Berry, C. Brabec, F. Brunetti, V. Bulović, Q. Burlingame, A. Di Carlo, R. Cheacharoen, Y.-B. Cheng, A. Colsmann, S. Cros, K. Domanski, M. Dusza, C. J. Fell, S. R. Forrest, Y. Galagan, D. Di Girolamo, M. Grätzel, A. Hagfeldt, E. von Hauff, H. Hoppe, J. Kettle, H. Köbler, M. S. Leite, S. Liu, Y.-L. Loo, J. M. Luther, C.-Q. Ma, M. Madsen, M. Manceau, M. Matheron, M. McGehee, R. Meitzner, M. K. Nazeeruddin, A. F. Nogueira, Ç. Odabaşı, A. Osherov, N.-G. Park, M. O. Reese, F. De Rossi, M. Saliba, U. S. Schubert, H. J. Snaith, S. D. Stranks, W. Tress, P. A. Troshin, V. Turkovic, S. Veenstra, I. Visoly-Fisher, A. Walsh, T. Watson, H. Xie, R. Yıldırım, S. M. Zakeeruddin, K. Zhu, and M. Lira-Cantu. Consensus statement for stability assessment and reporting for perovskite photovoltaics based on isos procedures. *Nature Energy*, 5(1):35–49, 2020.

[40] X. Zheng, B. Chen, M. Yang, C. Wu, B. Orler, R. B. Moore, K. Zhu, and S. Priya. The controlling mechanism for potential loss in $CH_3NH_3PbBr_3$ hybrid solar cells. *ACS Energy Letters*, 1(2):424–430, 2016.

[41] S. Shao, J. Liu, H.-H. Fang, L. Qiu, G. H. ten Brink, J. C. Hummelen, L. J. A. Koster, and M. A. Loi. Efficient perovskite solar cells over a broad temperature window: The role of the charge carrier extraction. *Advanced Energy Materials*, 7(22), 2017.

[42] R. Singh, H. Hu, T. Feeney, A. Diercks, F. Laufer, Y. Li, T. Duong, F. Schackmar, B. A. Nejand, and U. W. Paetzold. Danger in the dark: Stability of perovskite solar cells with varied stoichiometries and morphologies stressed at various conditions. *ACS Applied Materials & Interfaces*, 16(21):27450–27462, 2024.

[43] S. Reed in Financial Models Lab. 7 Critical KPIs for Solar Panel Manufacturing. `https://financialmodelslab.com/blogs/kpi-metrics/solar-panel-manufacturing`. accessed: June, 2026.

[44] M. Kim, G.-H. Kim, T. K. Lee, I. W. Choi, H. W. Choi, Y. Jo, Y. J. Yoon, J. W. Kim, J. Lee, D. Huh, H. Lee, S. K. Kwak, J. Y. Kim, and D. S. Kim. Methylammonium Chloride Induces Intermediate Phase Stabilization for Efficient Perovskite Solar Cells. *Joule*, 3(9):2179–2192, 2019.

[45] E. Gutierrez-Partida, H. Hempel, S. Caicedo-Dávila, M. Raoufi, F. Peña-Camargo, M. Grischek, R. Gunder, J. Diekmann, P. Caprioglio, K. O. Brinkmann, H. Köbler, S. Albrecht, T. Riedl, A. Abate, D. Abou-Ras, T. Unold, D. Neher, and M. Stolterfoht. Large-grain double cation perovskites with 18 μs lifetime and high luminescence yield for efficient inverted perovskite solar cells. *ACS Energy Letters*, 6(3):1045–1054, 2021.

[46] L. Krückemeier, U. Rau, M. Stolterfoht, and T. Kirchartz. How to Report Record Open-Circuit Voltages in Lead-Halide Perovskite Solar Cells. *Advanced Energy Materials*, 10(1):1902573, 2020.

[47] J. Wang, L. Yuan, H. Luo, C. Duan, B. Zhou, Q. Wen, and K. Yan. Ambient air processed highly oriented perovskite solar cells with efficiency exceeding 23% via amorphous intermediate. *Chemical Engineering Journal*, 446:136968, 2022.

[48] G. Zeng, G. Liu, and X. Li. Hexamethylphosphoramide-assisted structure and morphology regulation of a PbI_2 film for air-processed efficient perovskite solar cells via a two-step deposition method. *ACS Sustainable Chemistry & Engineering*, 2023.

[49] J. C. Fischer, C. Li, S. Hamer, L. Heinke, R. Herges, B. S. Richards, and I. A. Howard. Giwaxs characterization of metal-organic framework thin films and heterostructures: Quantifying structure and orientation. *Advanced Materials Interfaces*, 10(11), 2023.

[50] Z. Jiang. Gixsgui: a matlab toolbox for grazing-incidence x-ray scattering data visualization and reduction, and indexing of buried three-dimensional periodic nanostructured films. *Journal of Applied Crystallography*, 48(3):917–926, 2015.

[51] M. Stolterfoht, M. Grischek, P. Caprioglio, Ch. M. Wolff, E. Gutierrez-Partida, F. Peña-Camargo, D. Rothhardt, S. Zhang, M. Raoufi, J. Wolansky, M. Abdi-Jalebi, S. D. Stranks, St. Albrecht, Th. Kirchartz, and D. Neher. How to Quantify the Efficiency Potential of Neat Perovskite Films: Perovskite Semiconductors with an Implied Efficiency Exceeding 28%. *Advanced Materials*, 32(17):2000080, 2020.

[52] P. Fassl, V. Lami, F. J. Berger, L. M. Falk, J. Zaumseil, B. S. Richards, I. A. Howard, Y. Vaynzof, and U. W. Paetzold. Revealing the internal luminescence quantum efficiency of perovskite films via accurate quantification of photon recycling. *Matter*, 4(4):1391–1412, 2021.

[53] G. D. Ruxton. The unequal variance t-test is an underused alternative to student's t-test and the Mann–Whitney U test. *Behavioral Ecology*, 17(4):688–690, 2006.

[54] B. Derrick and P. White. Why Welch's test is Type i error robust. *The Quantitative Methods for Psychology*, 12(1):30–38, 2016.

[55] GraphPad by by Dotmatics. T test calculator. accessed: May, 2026.

Table of Contents

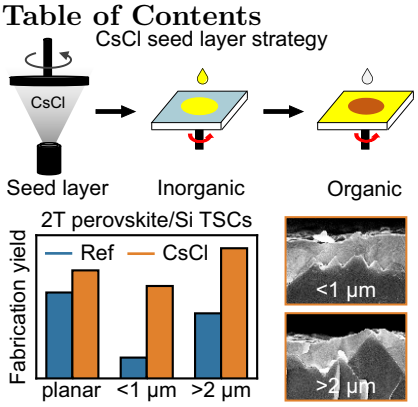

This study introduces a thin CsCl seed layer at the hole transport layer/perovskite interface in a solution-based two-step process as a simple and effective strategy to improve perovskite coverage on textured silicon surfaces. The CsCl seed layer strategy enhances fabrication yield, device performance and stability, highlighting its potential for industrially relevant perovskite/silicon tandem solar cell manufacturing.

Supporting Information

Table S1: Photovoltaic parameters of the champion opaque perovskite solar cells (PSCs) including the reference devices (Ref) and the devices with 5 nm CsCl (CsCl).

samples	scan direction	V_{OC} [V]	J_{SC} [mA/cm^2]	FF [%]	PCE [%]	HI [%][a]
Ref	backward	1.21	19.46	77.80	18.25	7.67
	forward	1.20	19.40	72.49	16.85	
CsCl	backward	1.20	19.71	80.38	19.03	5.47
	forward	1.20	19.72	76.36	17.99	

[a]Note: HI [%] = [(PCE at backward scan - PCE at forward scan)/PCE at backward scan] · 100.

Table S2: *Welch's t test* results for the backward power conversion efficiency (PCE), open-circuit voltage (V_{OC}), short-circuit current density (J_{SC}) and fill factor (FF) parameters of the opaque perovskite solar cells (PSCs) for the reference devices (Ref) and the devices with 5 nm CsCl (CsCl). The calculation was performed using a *t test* calulator.[55]

parameter	samples	P-value	interpretation difference
PCE	Ref and CsCl	0.0178	statistically significant
V_{OC}	Ref and CsCl	0.0046	very statistically significant
J_{SC}	Ref and CsCl	0.3610	not statistically significant
FF	Ref and CsCl	< 0.0001	extremely statistically significant

Table S3: Photovoltaic parameters (backward direction) of the champion semitransparent perovskite solar cells (PSCs) before and after 1000 h ISOS-D1 testing conditions for Ref and CsCl devices.

samples	scan direction	V_{OC} [V]	J_{SC} [mA/cm^2]	FF [%]	PCE [%]	HI [%][a]
Ref	before	1.20	18.55	74.74	16.61	5.78
	after	1.20	18.64	73.22	16.36	5.56
CsCl	before	1.19	18.94	72.41	16.27	5.90
	after	1.16	18.53	69.92	15.08	3.85

[a]Note: HI [%] = [(PCE at backward scan - PCE at forward scan)/PCE at backward scan] · 100.

Table S4: Photovoltaic parameters (backward direction) of the champion semitransparent perovskite solar cells (PSCs) before and after 1000 h ISOS-D2 testing conditions for Ref and CsCl devices.

samples	scan direction	V_{OC} [V]	J_{SC} [mA/cm^2]	FF [%]	PCE [%]	HI [%][a]
Ref	before	1.20	18.79	74.09	16.69	5.81
	after	1.12	5.42	35.08	2.12	3.58
CsCl	before	1.19	19.33	74.95	17.19	5.24
	after	1.10	5.98	35.51	2.33	0.43

[a]Note: HI [%] = [(PCE at backward scan - PCE at forward scan)/PCE at backward scan] · 100.

Table S5: Photovoltaic parameters (backward direction) of the champion semitransparent perovskite solar cells (PSCs) before and after 1000 h ISOS-L1 testing conditions for Ref and CsCl devices.

samples	scan direction	V_{OC} [V]	J_{SC} [mA/cm^2]	FF [%]	PCE [%]	HI [%][a]
Ref	before	1.19	18.23	78.11	16.96	6.43
	after	1.14	18.44	77.93	16.39	8.54
CsCl	before	1.18	18.77	77.81	17.21	6.91
	after	1.14	18.07	76.25	15.78	7.79

[a]Note: HI [%] = [(PCE at backward scan - PCE at forward scan)/PCE at backward scan] · 100.

Table S6: Statistical comparison of functional (not shunted) 2T perovskite/Si tandem solar cells (TSCs) for Ref and CsCl devices, evaluated over two fabrication batches comprising six cells per bottom cell type and parameter.

Si bottom cell	Ref	CsCl
planar	66%	83%
small texture	16%	71%
large texture	50%	100%

Table S7: Performance of 2T perovskite/Si tandem solar cells (TSCs) for Ref and CsCl devices from Batch 1. Only the power conversion efficiency (PCE) in backward scan direction is shown. The solution-based two-step process has not been optimized for tandem integration and requires further refinement to improve device performance.

samples	Si bottom cell		
	planar	small texture	large texture
Ref	-	22.0%	21.2%
	-	-	20.9%
	25.2%	-	-
CsCl	23.1%	-	22.8%
	26.8%	20.9%	14.9%
	-	-	22.8%

Table S8: Performance of 2T perovskite/Si tandem solar cells (TSCs) for Ref and CsCl devices from Batch 2. Only the power conversion efficiency (PCE) in backward scan direction is shown. The solution-based two-step process has not been optimized for tandem integration and requires further refinement to improve device performance.

samples	Si bottom cell		
	planar	small texture	large texture
Ref	21.0%	-	-
	15.6%	-	18.8%
	21.0%	-	-
CsCl	21.0%	16.4%	14.4%
	21.1%	17.0%	15.1%
	19.8%	18.6%	13.2%

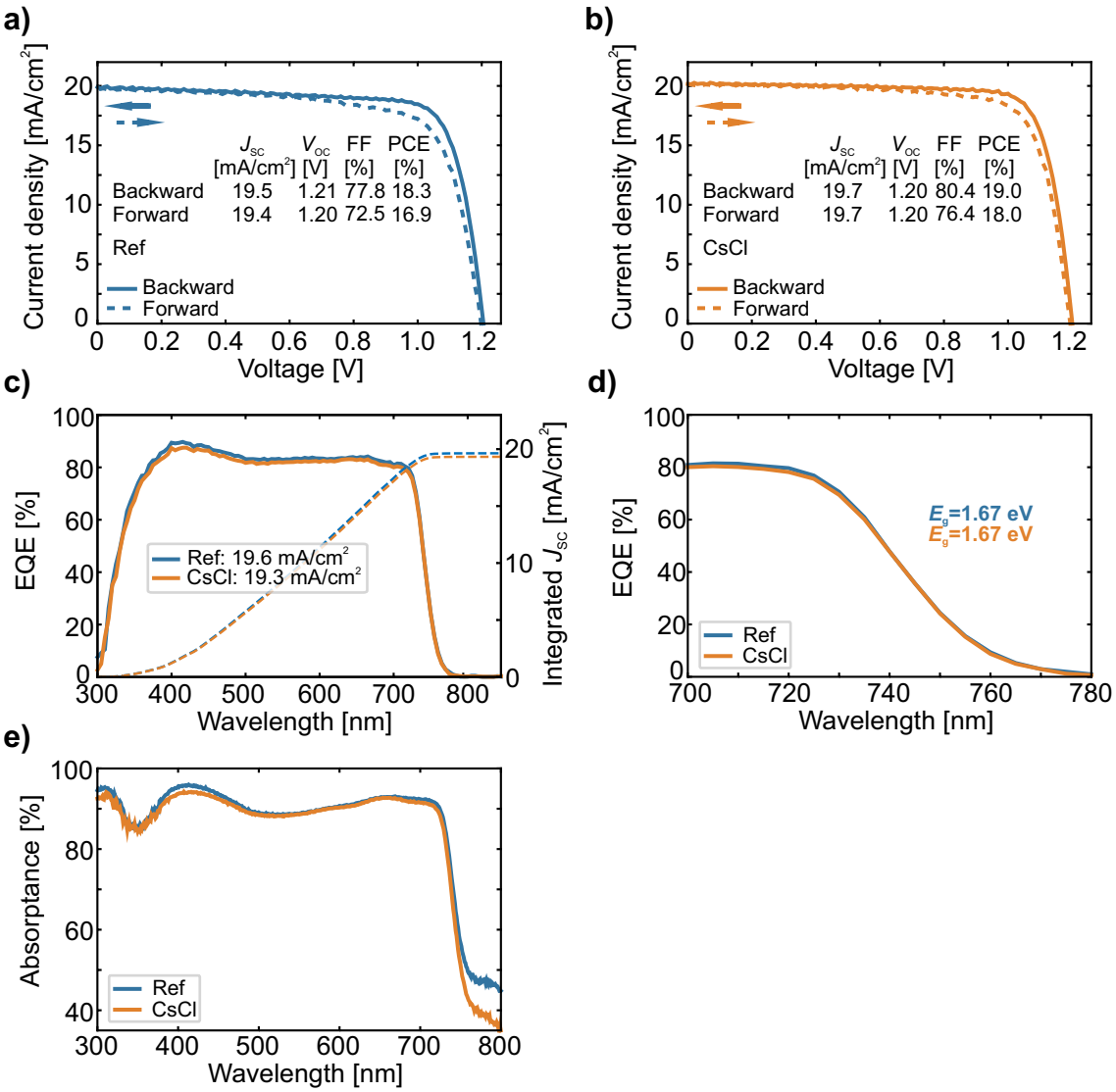

Figure S1: Current density *versus* voltage (J–V) characteristics of champion opaque perovskite solar cells (PSCs) a) without any further modification (Ref) and b) with 5nm CsCl seed layer (CsCl). c) External quantum efficiency (EQE) as well as the corresponding integrated J_{SC}, d) optical bandgap extracted from the inflection point of the EQE spectra and e) absorptance spectra for Ref and CsCl PSCs.

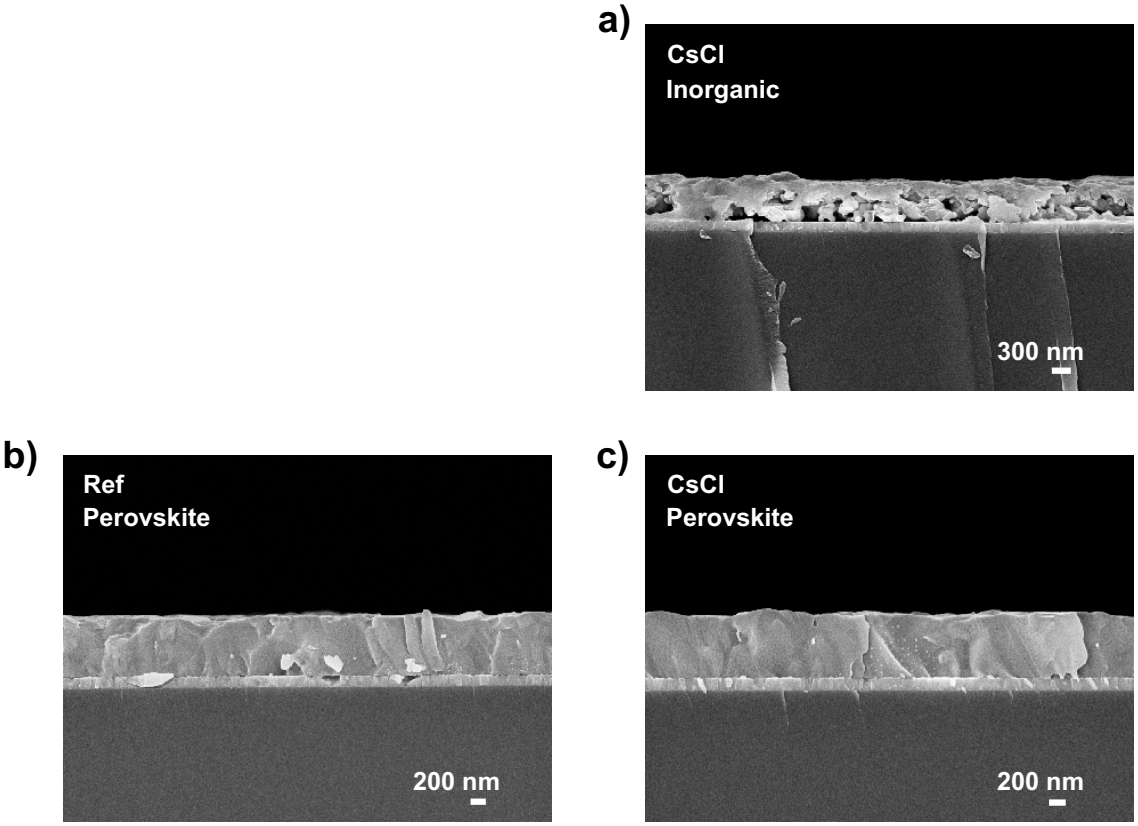

Figure S2: Representative cross-sectional scanning electron microscopy (SEM) images of an inorganic scaffold with 5nm CsCl seed layer (CsCl), and perovskite films b) without any further modification (Ref) and c) with 5nm CsCl seed layer (CsCl). The inorganic scaffolds and perovskite films are prepared on ITO/NiO_x/2PACz substrates. The perovskite films are without surface passivation. Unfortunately, it was not possible to focus on the inorganic scaffold, which is why no image can be shown.

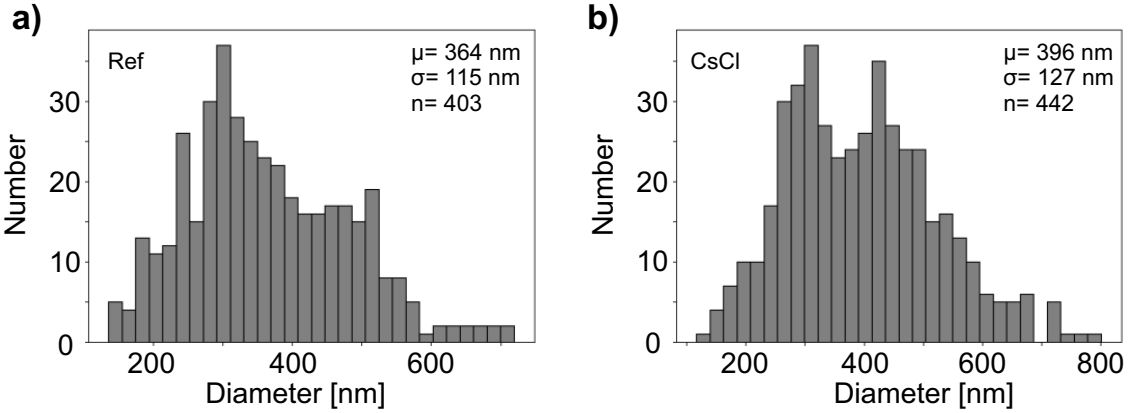

Figure S3: Grain size analysis of scanning electron microscopy (SEM) images of perovskite films a) without any further modification (Ref), and b) with 5nm CsCl seed layer (CsCl). The perovskite films are without surface passivation. The grain sizes were determined using an analysis software based on StarDist.

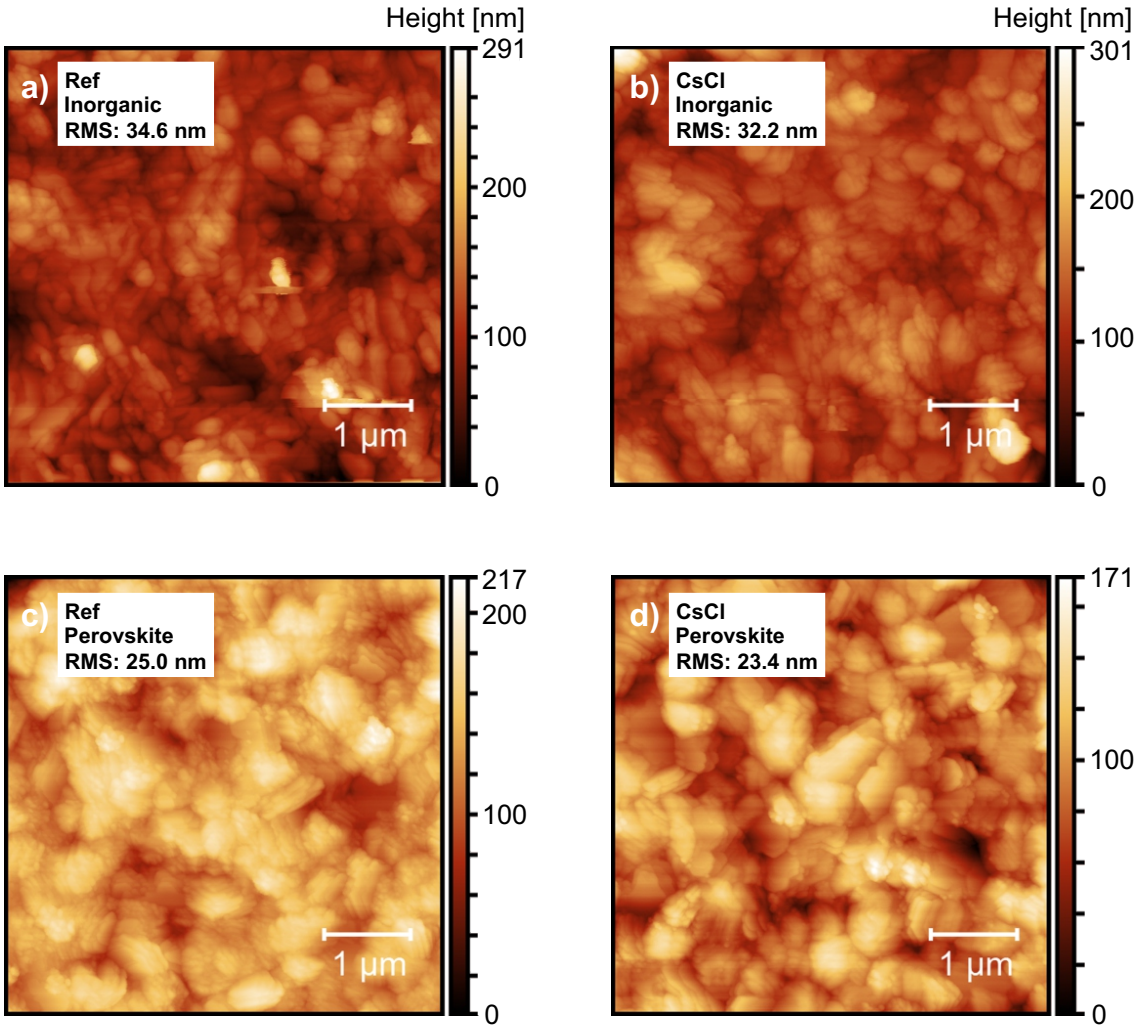

Figure S4: Representative atomic force microscopy (AFM) analysis of inorganic scaffolds a) without any further modification (Ref) and b) with 5nm CsCl seed layer (CsCl), and of perovskite films c) without any further modification (Ref), and d) with 5nm CsCl seed layer (CsCl). The inorganic scaffolds and perovskite films are prepared on ITO/NiO_x/2PACz substrates. The perovskite films are without surface passivation. The average root-mean-square (RMS) value was determined from 2-3 measurements.

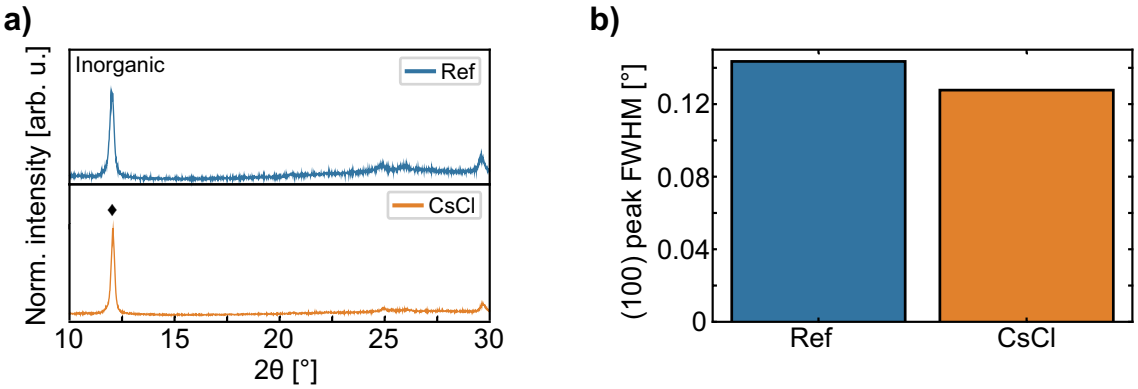

Figure S5: a) X-ray diffraction (XRD) pattern of inorganic scaffolds without any further modification (Ref) and with 5nm CsCl seed layer (CsCl) (♦ denotes the (001) PbI_2 phase). b) Full width at half maximum (FWHM) of the (100) perovskite peak for Ref and CsCl perovskite films. The inorganic scaffolds and perovskite films are prepared on ITO/NiO_x/2PACz substrates. The perovskite films are without surface passivation.

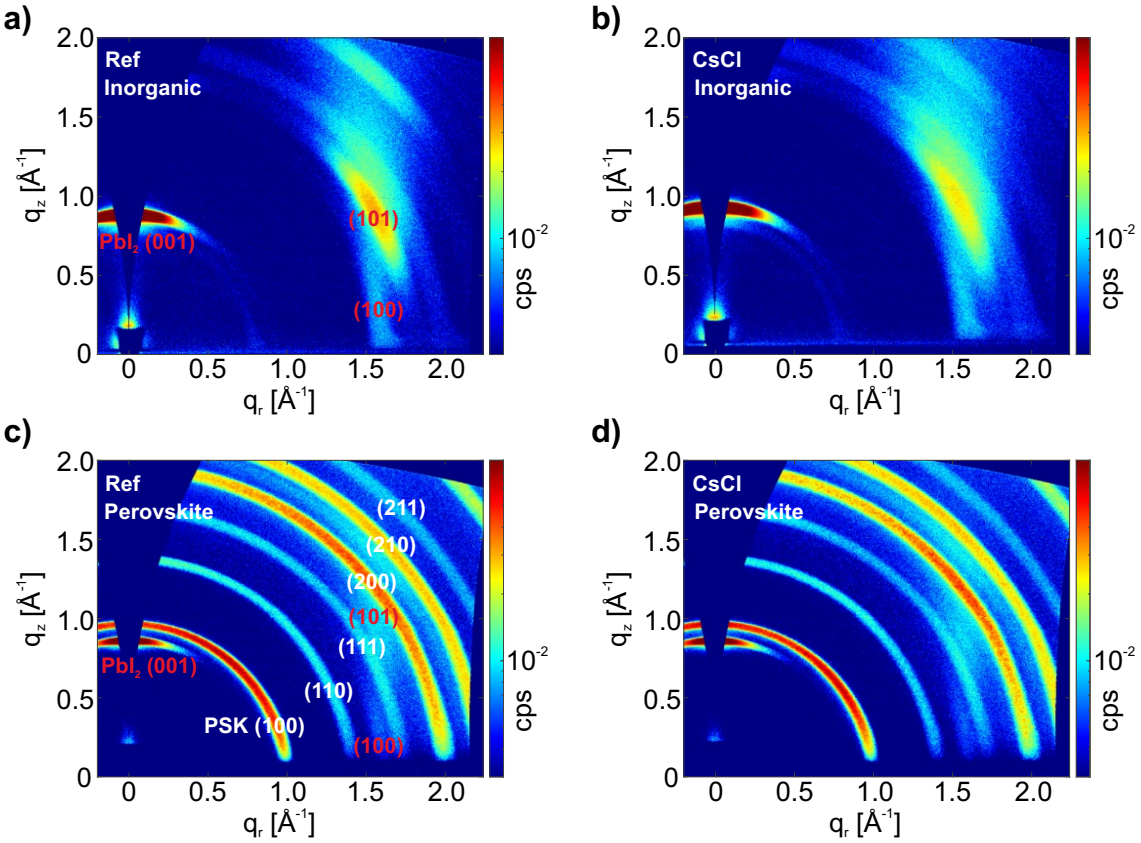

Figure S6: Grazing-incidence wide-angle scattering (GIWAXS) patterns of a/b) inorganic scaffolds and c/d) perovskite films without any further modification (Ref), and with 5nm CsCl seed layer (CsCl). The inorganic scaffolds and perovskite films are prepared on ITO/NiO_x/2PACz substrates. The perovskite films are without surface passivation.

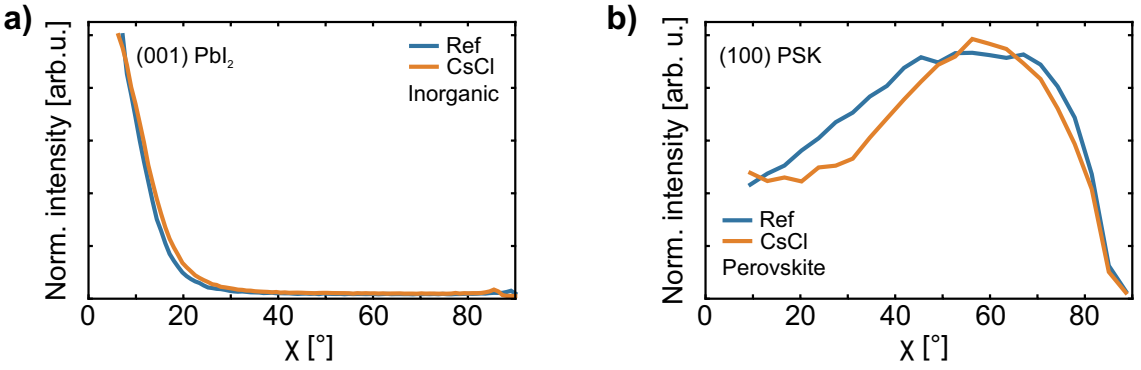

Figure S7: Pole figure of the a) (001) PbI_2 peak for inorganic scaffolds and b) (100) perovskite peak for perovskite films without any further modification (Ref) and with 5nm CsCl seed layer (CsCl). The inorganic scaffolds and perovskite films are prepared on ITO/NiO_x/2PACz substrates. The perovskite films are without surface passivation.

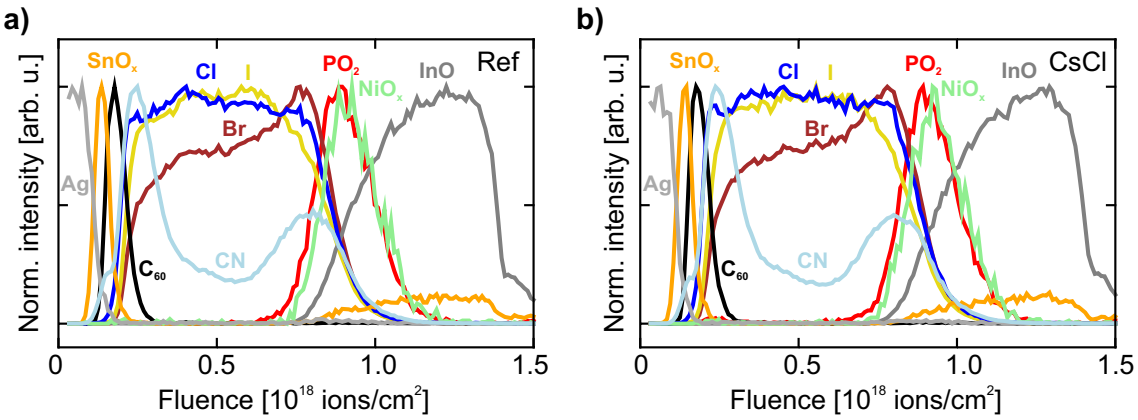

Figure S8: Normalized time-of-flight secondary ion mass spectrometry (ToF-SIMS) measurements (negative polarity) of perovskite solar cells (PSCs) a) without any further modification (Ref) and b) with 5nm CsCl seed layer (CsCl). The PSCs have the layer stack glass/ITO/NiO_x/2PACz/perovskite/ $PDAI_2$+BAI/C_{60}/SnO_2/Ag. The following fragments are displayed: InO: $^{115}InO^-$; NiO: NiO^-; PO_2: PO_2^-; I: I^-; Cl: $\Sigma(^{35}Cl^-, ^{37}Cl^-)$; Br: $^{81}Br^-$; CN: CN^-; C_{60}: $\Sigma(C_3^-, C_4^-, C_6^-)$; SnO_x: $\Sigma(^{116}SnO^-, ^{118}SnO^-, ^{120}SnO^-)$; Ag: $\Sigma(^{107}AgO^-, ^{109}AgO^-)$.

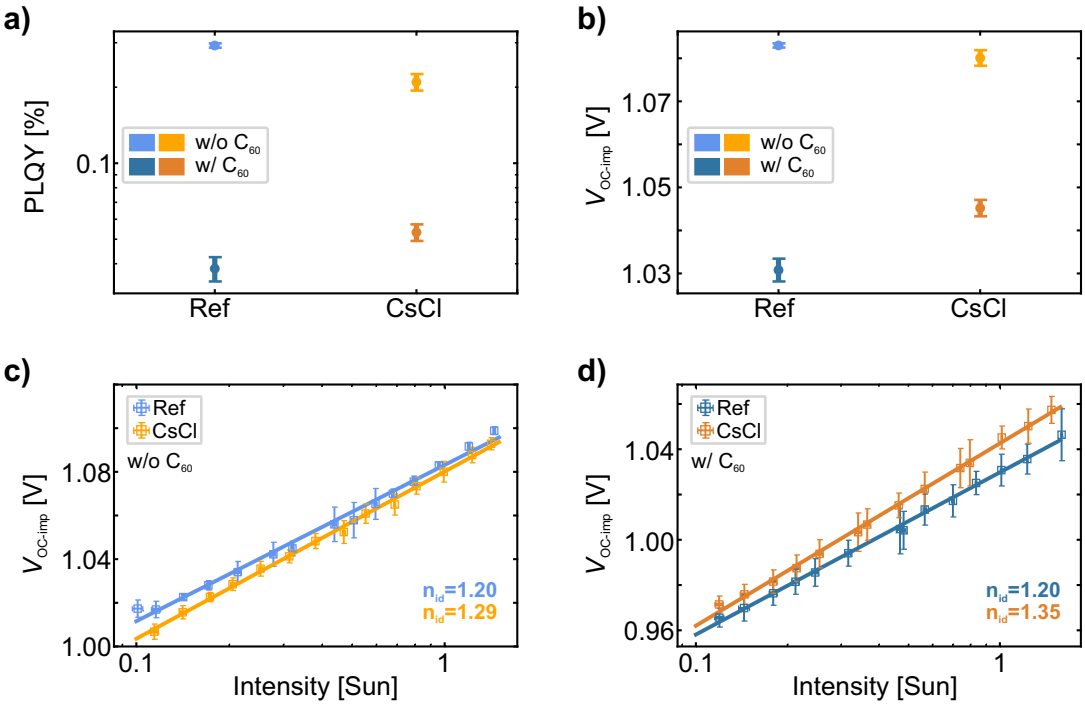

Figure S9: a) Photoluminescence quantum yield (PLQY), b) the obtained implied V_{OC} (V_{OC-imp}), and the ideality factor (n_{id}) extracted from a fit to the V_{OC-imp} (derived from intensity-dependent PLQY measurements) measured a) without and b) with C_{60} electron transport layer (ETL) of perovskite films without any further modification (Ref) and with 5 nm CsCl seed layer (CsCl) fabricated on glass/indium tin oxide (ITO)/NiO_x/2PACz. All perovskite films have $PDAI_2$+BAI as surface passivation. PLQY is measured from the hole transport layer (HTL) side. For each parameter, several perovskite films are measured, and the corresponding mean and standard deviation are plotted.

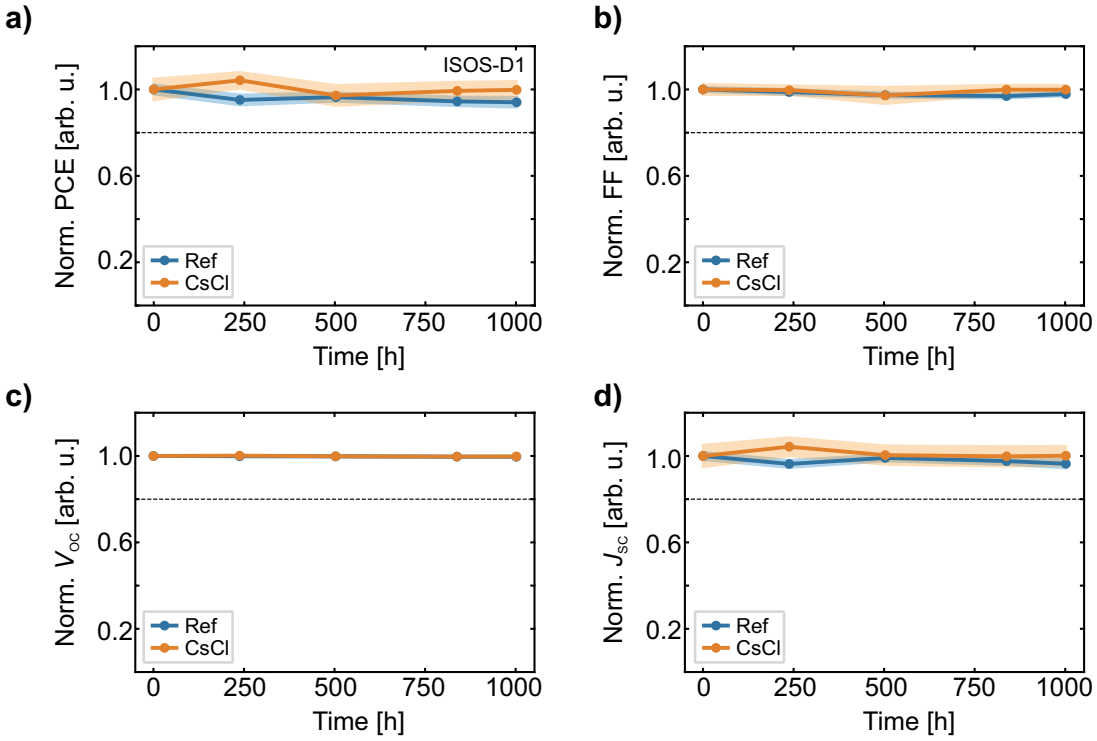

Figure S10: Normalized a) power conversion efficiency (PCE), b) fill factor (FF), c) open-circuit voltage (V_{OC}), and d) short-circuit current density (J_{SC}) from J–V measurements of semitransparent perovskite solar cells (PSCs) without any further modification (Ref) and with 5nm CsCl seed layer (CsCl) under ISOS-D1 testing conditions (dark, intermittent J–V) for 1000 h. Mean values and standard deviations based on twelve devices per parameter are provided.

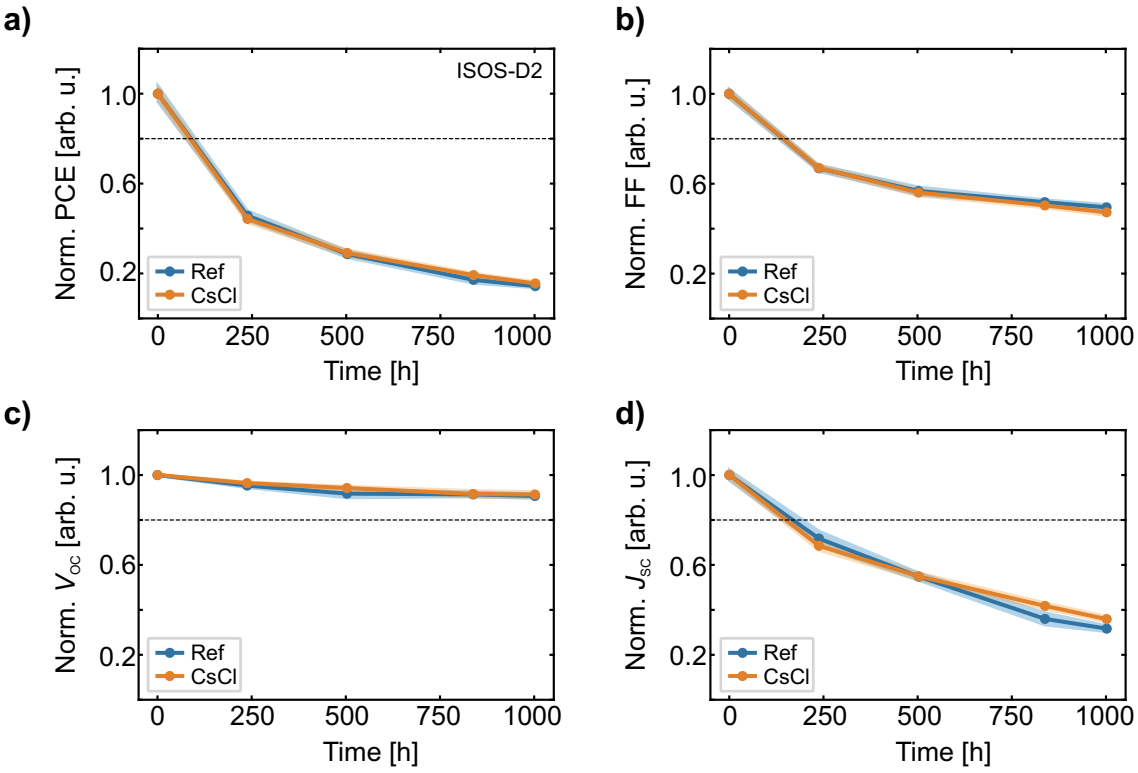

Figure S11: Normalized a) power conversion efficiency (PCE), b) fill factor (FF), c) open-circuit voltage (V_{OC}), and d) short-circuit current density (J_{SC}) from J–V measurements of semitransparent perovskite solar cells (PSCs) without any further modification (Ref) and with 5nm CsCl seed layer (CsCl) under ISOS-D2 testing conditions (dark, 85 °C, intermittent J–V) for 1000 h. Mean values and standard deviations based on twelve devices per parameter are provided.

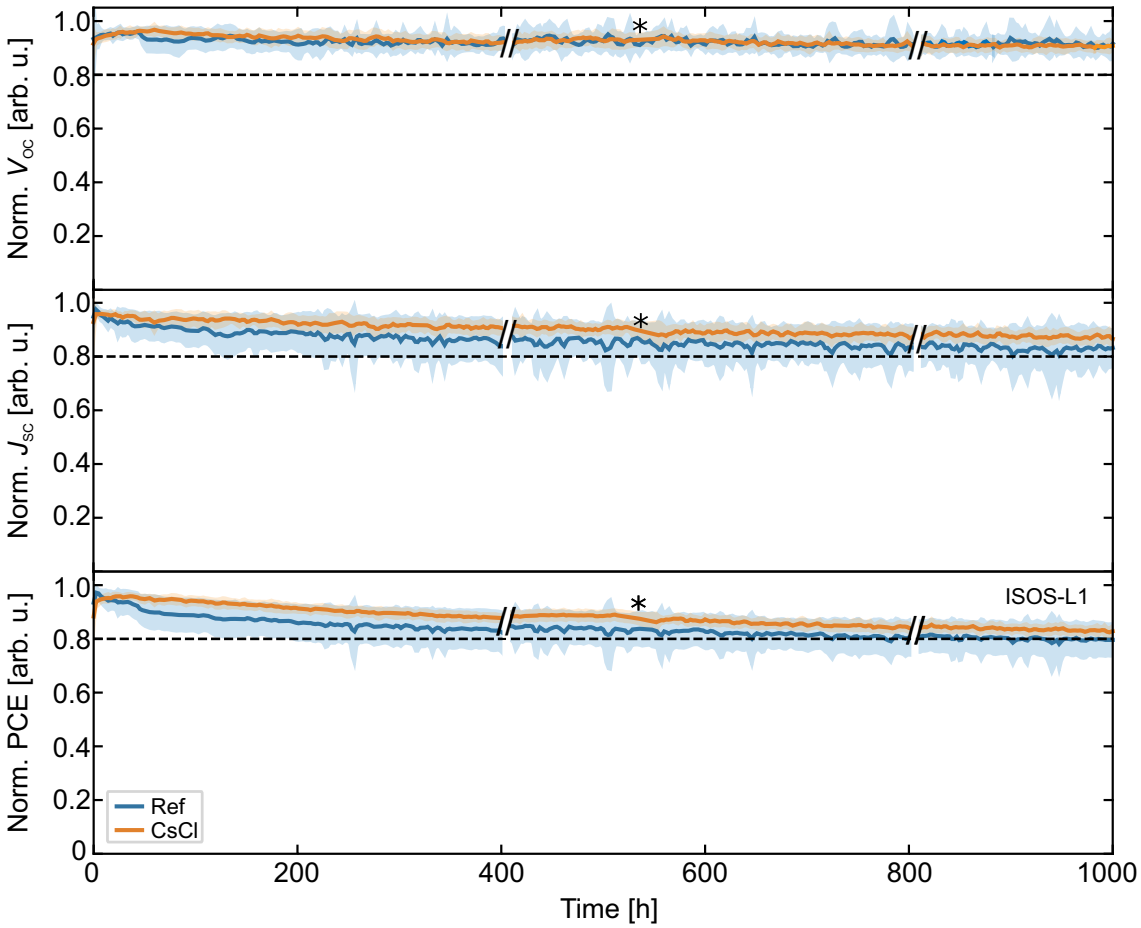

Figure S12: Normalized open-circuit voltage (V_{OC}), short-circuit current density (J_{SC}) and power conversion efficiency (PCE) at the maximum power point (MPP) tracking of semitransparent perovskite solar cells (PSCs) without any further modification (Ref) and with 5nm CsCl seed layer (CsCl) under ISOS-L1 test conditions (100 mW/cm^2, 25 °C, MPP tracking) for 1000 h. Mean values and standard deviations based on 10-14 devices per parameter are provided. The data fluctuations originate from the measurement setup. // indicates brief periods when the solar simulator lamp was turned off, while * marks a short interruption in the measurement. To account for these pauses, the measurement duration was extended, ensuring a total exposure time of 1000 h.

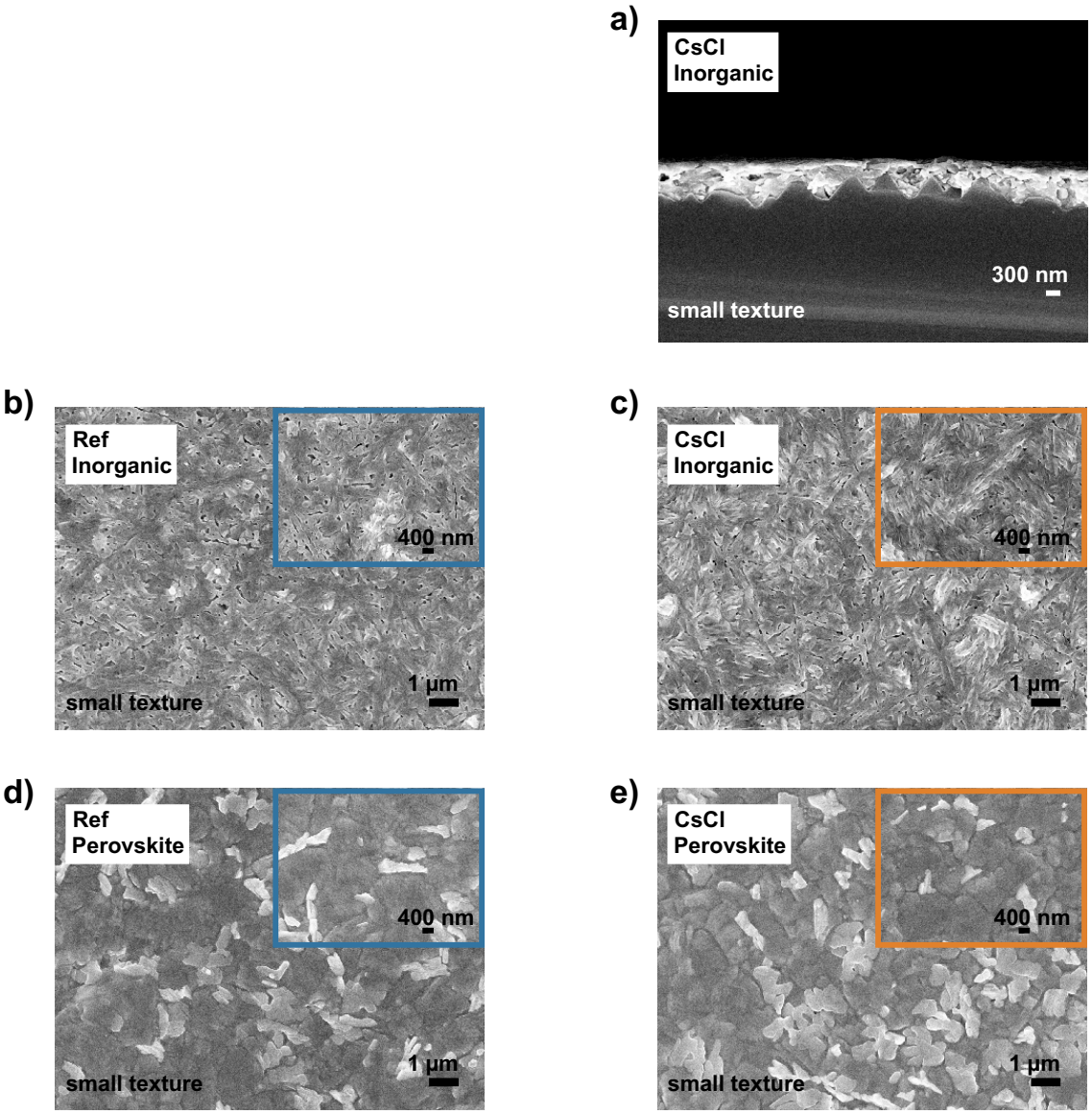

Figure S13: a) Representative cross-sectional scanning electron microscopy (SEM) image of the inorganic scaffold with 5 nm CsCl seed layer (CsCl). Unfortunately, it was not possible to focus on the Ref inorganic scaffold, which is why no image can be shown. Representative top-view SEM images of inorganic scaffolds and perovskite films b/d) without any further modification (Ref) and c/e) with 5 nm CsCl seed layer (CsCl) on small-textured silicon (Si) bottom cells (pyramid height $\approx$ 0.5-1 µm). The inorganic scaffold and perovskite films are prepared on Si/indium tin oxide (ITO)/NiO_x/2PACz. The perovskite films are without surface passivation.

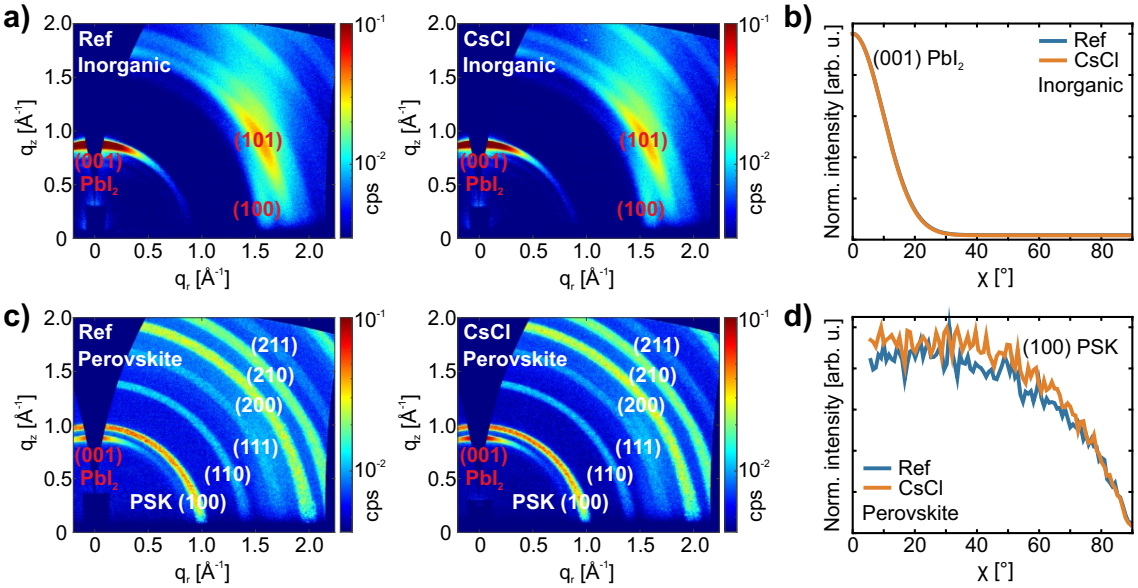

Figure S14: Grazing-incidence wide-angle scattering (GIWAXS) patterns of a) inorganic scaffolds, and c) perovskite films, and the corresponding pole figures of the b) (100) PbI_2 phase for inorganic scaffolds, and the d) (100) perovskite (PSK) phase for perovskite films without any further modification (Ref) and with 5 nm CsCl seed layer (CsCl) on small-textured silicon (Si) bottom cells (pyramid height ≈ 0.5-1 µm). The inorganic scaffolds and perovskite films are prepared on Si/indium tin oxide (ITO)/NiO_x/2PACz. The perovskite films are without surface passivation.

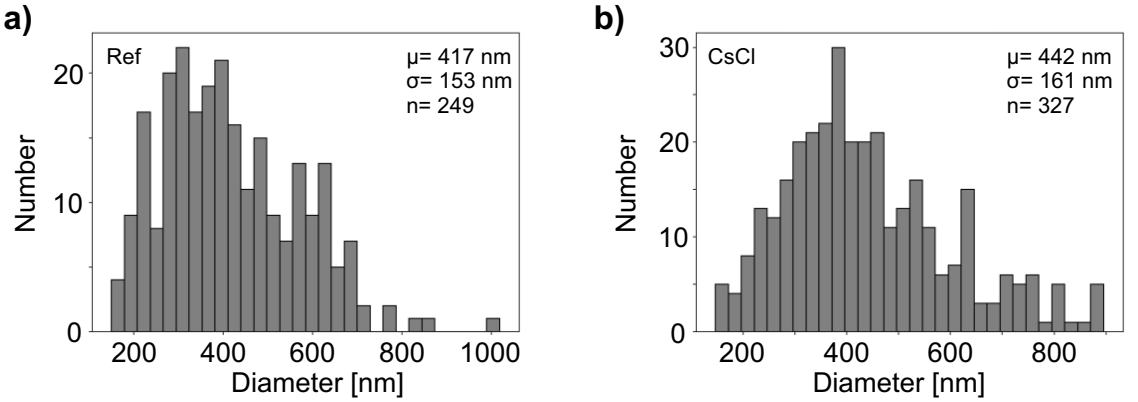

Figure S15: Grain size analysis of scanning electron microscopy (SEM) images of perovskite films on small-textured silicon (Si) bottom cells (pyramid height ≈ 0.5-1 µm) a) without any further modification (Ref), and b) with 5 nm CsCl seed layer (CsCl). The perovskite films are without surface passivation. The grain sizes were determined using an analysis software based on StarDist.

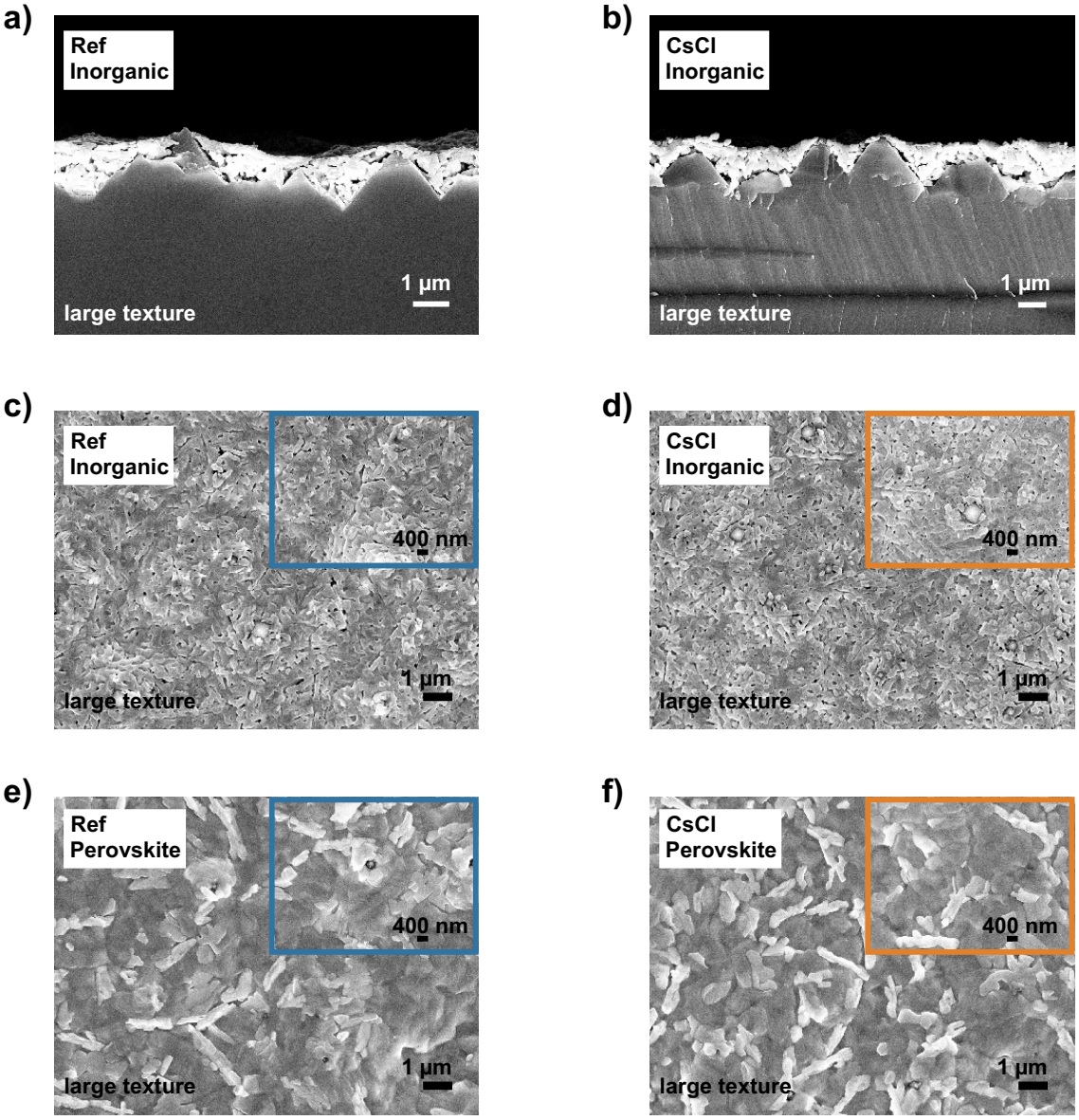

Figure S16: Representative cross-sectional scanning electron microscopy (SEM) image of the inorganic scaffold a) without any further modification (Ref) and b) with 5 nm CsCl seed layer (CsCl). Representative top-view SEM images of inorganic scaffolds and perovskite films b/d) without any further modification (Ref) and c/e) with 5 nm CsCl seed layer (CsCl) on large-textured silicon (Si) bottom cells (pyramid height ≈ 2-5 µm). The inorganic scaffold and perovskite films are prepared on Si/indium tin oxide (ITO)/NiO_x/2PACz. The perovskite films are without surface passivation.

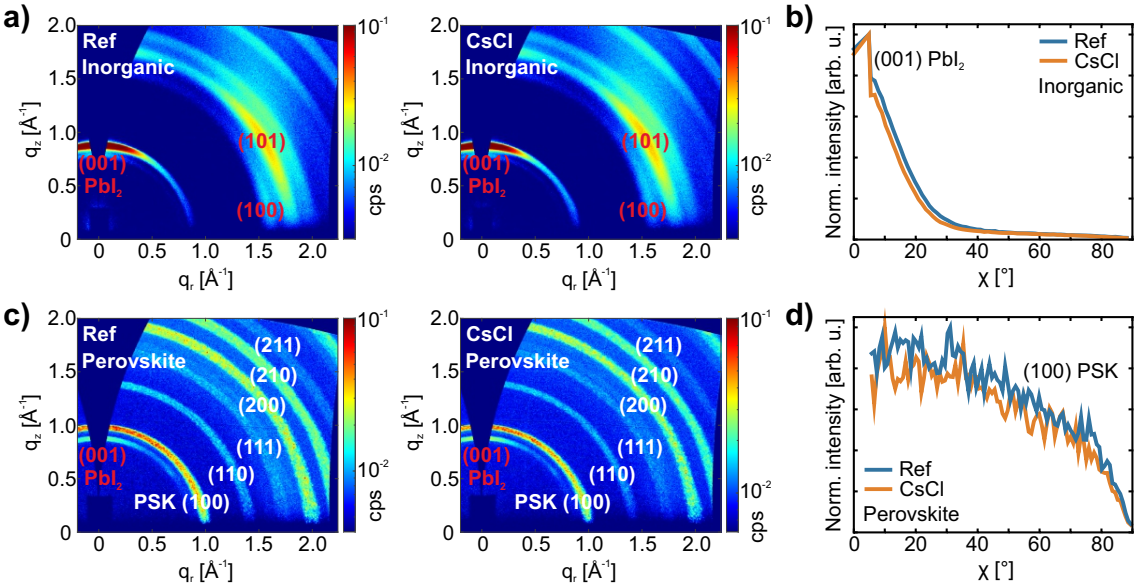

Figure S17: Grazing-incidence wide-angle scattering (GIWAXS) patterns of a) inorganic scaffolds, and c) perovskite films, and the corresponding pole figures of the b) (100) PbI_2 phase for inorganic scaffolds, and the d) (100) perovskite (PSK) phase for perovskite films without any further modification (Ref) and with 5 nm CsCl seed layer (CsCl) on large-textured silicon (Si) bottom cells (pyramid height ≈ 2-5 µm). The inorganic scaffolds and perovskite films are prepared on Si/indium tin oxide (ITO)/NiO_x/2PACz. The perovskite films are without surface passivation.

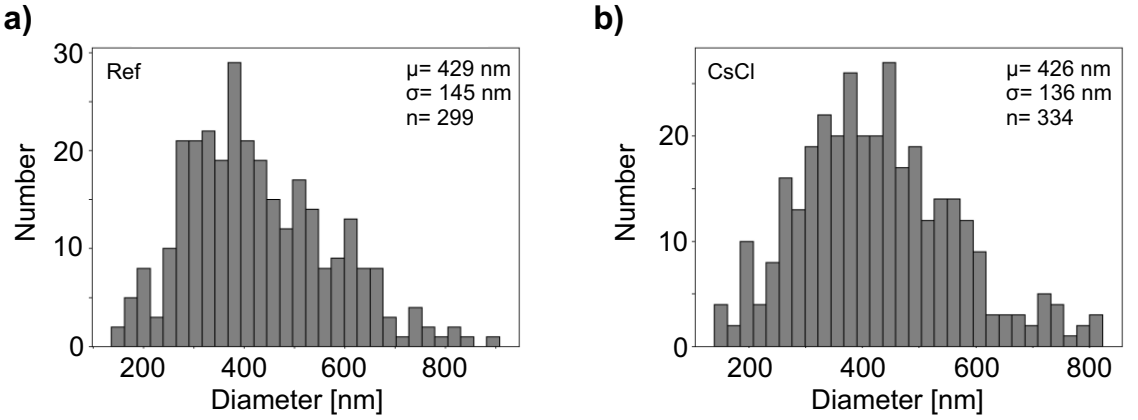

Figure S18: Grain size analysis of scanning electron microscopy (SEM) images of perovskite films on large-textured silicon (Si) bottom cells (pyramid height ≈ 2-5 µm) a) without any further modification (Ref) and b) with 5 nm CsCl seed layer (CsCl). The perovskite films are without surface passivation. The grain sizes were determined using an analysis software based on StarDist.

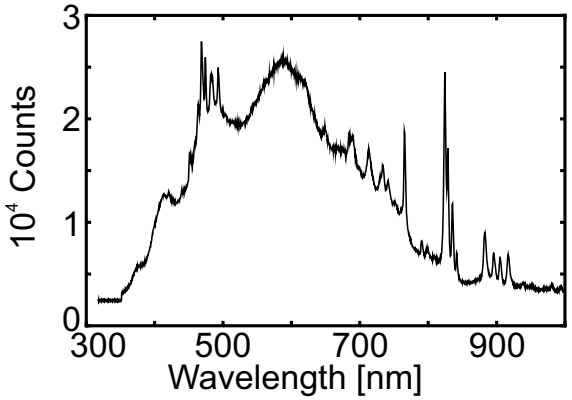

Figure S19: Spectrum of the class AAA xenon-lamp solar simulator (Newport Oriel Sol3A) used to measure J–V and maximum power point (MPP) curves.